of adult HSCs [13]. Furthermore, VEGF has been shown to be an essential factor for HSC niche formation through endochondral ossification [14]. These observations clearly demonstrate that VEGF exerts physiological actions on hematopoietic systems through both cell-autonomous and -nonautonomous mechanisms.

In addition to the functions described above, VEGF also has a potent HSPC mobilization capacity [15], although the mechanisms of VEGF-induced HSPC mobilization have not been addressed in detail. In the current study, we investigated the effect of VEGF on the BM cell mobilization and BM environment after the intravenous injection of VEGF-expressing adenovirus (Ad) vector (Ad-VEGF) into mice. The results showed that VEGF overexpression in mice could lead to a reduction of not only the HPSC number, but also the MPC number in the BM. We also observed an enhanced chemoattractive activity of BM stromal cells by VEGF. Our data suggest that the plasma elevation of VEGF in mice alters the distribution of MPCs in the BM, and this might cause HSPC egress from the BM.

Materials and Methods

Ad vectors

Ad vectors were constructed by an improved in vitro ligation method [16,17]. The mouse $VEGF_{165}$ cDNA and human G-CSF cDNA were obtained from pBLAST49-mVEGF and pORF9-hGCSFb, respectively (Invivogen). Each cDNA was cloned into a multicloning site of pHMCMV10 [18,19], which contains the cytomegalovirus (CMV) promoter/enhancer and intron A sequence flanked by the I-*Ceu*I and PI-*Sce*I sites, thereby resulting in pHMCMV10-VEGF and pHMCMV10-G-CSF. pHMCMV10-VEGF and pHMCMV10-G-CSF were digested with I-*Ceu*I/PI-*Sce*I and ligated into I-*Ceu*I/PI-*Sce*I-digested pAdHM41-K7 (C) [20], resulting in pAd-VEGF and pAd-G-CSF, respectively. To generate the virus, Ad vector plasmids were digested with *Pac*I and purified by phenol–chloroform extraction and ethanol precipitation. Linearized DNAs were transfected into 293 cells with SuperFect (Qiagen) according to the manufacturer's instructions. The viruses were amplified in 293 cells. Before virus purification, the cell lysates were centrifuged to remove cell debris and were digested for 30 min at 37°C with 200 μg/mL DNase I and 200 μg/mL RNase A in the presence of 10 mM $MgCl_2$. Viruses were purified by $CsCl_2$ step gradient ultracentrifugation followed by $CsCl_2$ linear gradient ultracentrifugation. The purified viruses were dialyzed against a solution containing 10 mM Tris-HCl (pH 7.5), 1 mM $MgCl_2$, and 10% glycerol and were stored at −80°C. The control vector, Ad-Null, is similar in design, except that it contains no transgene in the expression cassette. The biological titers [infectious unit (ifu)] of Ad-VEGF, Ad-G-CSF, and Ad-Null were determined by using an Adeno-X Rapid Titer kit (Clontech).

Administration of Ad vectors in mice

C57BL/6j female mice aged 7–9 weeks were obtained from Nippon SLC, and all animals were maintained under specific pathogen-free conditions. Each Ad vector was intravenously injected into C57BL/6j mice at 1×10^9 ifu through the tail vein. All experiments were conducted according to the institutional ethics guidelines for animal experimentation of the National Institute of Biomedical Innovation.

Cell preparation

Blood and BM were harvested from mice using standard methods on day 5 after injection of Ad vector into mice, and the number of nucleated cells in these tissues was then counted using a Nuclecounter (Chemometec). To collect the nonhematopoietic cells from the femur and tibia, the bone fragments were minced with scissors, and were then incubated at 37°C with a type I collagenase (3 mg/mL; Worthington) in the Dulbecco's modified Eagle's medium (DMEM) with 10% fetal bovine serum (FBS) for 90 min [21]. The cells were filtered with a cell strainer to remove debris and bone fragments, and suspended in a staining buffer [phosphate buffer saline (PBS)/2% FBS]. These cell suspensions were kept on ice for further analysis.

Flow cytometry

The following antibodies (Abs), conjugated with fluorescein isothiocyanate (FITC), phycoerythrin (PE), allophycocyanin (APC), or PECy7, were used for flow cytometric analysis and cell sorting: biotinylated lineage cocktail [CD3 (145-2C11), B220 (RA3-6B2), Gr-1 (RB6-8C5), CD11b (M1/70), Ter119 (Ter-119)], c-Kit-APC (2B8), Sca-1-PECy7 (D7), Ter119-FITC (Ter-119), CD45-FITC (30-F11), CD11b-FITC (M1/70), Gr-1-PE (RB6-8C5), CD31-FITC (390), CD31-APC (390), CD51-PE (RMV-7), PDGFRa-APC (APA-5), Flt-1-PE (141522), Flk1-PE (Avas12a1), and Alcam-PE. For detection of biotinylated Abs, PerCP-Cy5.5- or FITC-conjugated streptavidin was used. Abs were purchased from e-Bioscience, BD Bioscience, Biolegend, and R&D Systems. Cells were incubated with primary Abs at 4°C for 30 min and washed twice with PBS/2% FBS. After staining, cells were analyzed and isolated by flow cytometry on an LSR II and FACSAria flow cytometer, respectively, using FACSDiva software (BD Bioscience).

Enzyme linked immunosorbent assay

Blood samples were collected through the inferior vena cava on day 5 after Ad vector injection, and transferred to polypropylene tubes containing heparin. Plasma was harvested by centrifugation. The BM supernatant was obtained by flushing a femur with 500 μL of PBS, followed by centrifugation at 500*g* for 5 min. The levels of VEGF and CXCL12 in the plasma and BM supernatant were measured using a commercial ELISA kit (R&D Systems) following the manufacturer's instructions.

Reverse transcription-polymerase chain reaction analysis

CD45-negative($^-$) $Ter119^-$ nonhematopoietic cells in the BM were sorted from mice injected with Ad-VEGF or Ad-Null, and total RNA was then extracted using ISOGEN (Nippon Gene). cDNA was synthesized from DNase I-treated total RNA with a Superscript VILO cDNA synthesis kit

(Invitrogen), and quantitative real-time reverse transcription-polymerase chain reaction was performed using the Fast SYBR Green Master Mix with an ABI StepOne Plus system (Applied Biosystems). Relative quantification was performed against a standard curve and the values were normalized against the input determined for the housekeeping gene, glyceraldehyde 3-phosphate dehydrogenase. The sequences of the primers used in this study are listed in Table 1.

Colony assay

BM cells (2×10^4 cells) and peripheral blood cells (2×10^5 cells) were plated in the Methocult M3434 medium (StemCell Technologies, Inc.). Cultures were plated in duplicate and placed in a humidified chamber with 5% CO_2 at 37°C for 10 days. The number of individual colonies was counted by microscopy. The colony number was normalized to the total number of the nucleated cells.

Colony forming unit-fibroblast assay

BM-derived $CD45^-Ter119^-$ cells were added to the MesenCult MSC Basal Medium, including supplements (Stem Cell Technologies, Inc.), and then plated on a six-well plate at 1×10^5 cells per well. Cells were cultured for 14 days and stromal cell colonies (fibroblast-like colonies: >50 cells) derived from colony forming unit-fibroblasts (CFU-Fs) were stained with the Giemsa solution (Wako) after fixation with methanol. The colony number was counted by microscopy.

Cell migration assay

BM-derived stromal cells, including MPCs, were tested for migration toward VEGF using 8-μm pore-sized cell culture inserts (BD Falcon). Stromal cells (1×10^5 cells) resuspended in 200 μL of DMEM/2% FBS were added to the upper chamber, and 750 μL of DMEM/2% FBS containing recombinant mouse VEGF (10 or 100 ng/mL; Peprotech) was added to the bottom chamber. After 6 h of incubation at 37°C, the upper side of the filters was carefully washed with PBS, and cells remaining on the upper face of the filters were removed with a cotton wool swab. The filters were fixed with 100% methanol and stained with the Giemsa solution. Cells migrating into the lower compartment were counted manually in three random microscopic fields (×200).

Homing assay

Mice were administrated with Ad-Null or Ad-VEGF at 1×10^9 ifu. Five days later, BM cells (1×10^7 cells) derived from green fluorescent protein (GFP)-expressing transgenic mice [22] were intravenously transplanted into Ad-Null- or Ad-VEGF-injected mice. At 16 h after BM transplantation, the percentage of GFP-expressing donor cells in the BM was determined by flow cytometry.

Results

Effect of systemic VEGF overexpression on the distribution of myeloid cells and HSPCs in mice

To evaluate the effect of VEGF on the mobilization of hematopoietic cells, we generated a VEGF-expressing Ad vector, Ad-VEGF, because plasma VEGF levels were rapidly decreased with a $t_{1/2}$ of ~25 min after intravenous injection of recombinant VEGF [23]. Single intravenous injection of Ad-VEGF (1×10^9 ifu) into mice led to a significant elevation of VEGF levels in plasma on day 5 compared with Ad-Null-injected mice (control mice) (Fig. 1a). On the other hand, unexpectedly, BM VEGF levels in the Ad-VEGF-injected mice were almost equivalent to those in the Ad-Null-injected mice (Fig. 1b). There were no signs of toxicity in mice treated with Ad-VEGF and Ad-Null at this dose (1×10^9 ifu). To investigate whether the hematopoietic cells could be mobilized from the BM into the circulation after injection of Ad-VEGF, we examined the number of total nucleated cells, myeloid cells ($Gr\text{-}1^+CD11b^+$ cells), and HSPCs [$c\text{-}Kit^+Sca\text{-}1^+Lineage^-$ (KSL) cells or CFU-granulocyte, erythroid, macrophage, megakaryocyte/CFU-Mix] in the peripheral blood. Compared with Ad-Null-injected mice, Ad-VEGF-injected mice showed an increased number of total nucleated cells and myeloid cells in the peripheral blood (Fig. 1c, d). We found that the number of multipotent hematopoietic progenitor cells, CFU-GEMM/CFU-Mix, in the blood of Ad-VEGF-injected mice was four times as great as that of Ad-Null-injected mice (Fig. 1e). Importantly, in Ad-VEGF-injected mice, the number of KSL cells in the blood was also increased (Fig. 1f). These results indicate that hematopoietic cells, including immature hematopoietic cells with colony-forming potentials, would be mobilized from the BM following systemic Ad-VEGF administration.

An increased number of mobilized cells in VEGF-treated mice were reported previously [15], but little is known about the effect of VEGF on BM cells during the mobilization period. Thus, we next investigated the number of total BM cells, myeloid cells, and HSPCs. In contrast to the peripheral blood, the number of total hematopoietic cells, myeloid cells, and CFU-Mix was significantly decreased (Fig. 2a–c). It is of note that the VEGF overexpression in mice resulted

TABLE 1. PRIMER SEQUENCES USED IN THIS STUDY

Gene name	*(5′) Sense primers (3′)*	*(5′) Antisense primers (3′)*
Gapdh	TTCACCACCATGGAGAAGAAGGC	GGCATGGACTGTGGTCATGA
Cdh2	CAAGAGCTTGTCAGAATCAGG	CATTTGGATCATCCGCATC
Vcam-1	GACCTGTTCCAGCGAGGGTCTA	CTTCCATCCTCATAGCAATTAAGGTG
Angpt1	CTCGTCAGACATTCATCATCCAG	CACCTTCTTTTAGTGCAAAGGCT
Thpo	GGCCATGCTTCTTGCAGTG	AGTCGGCTGTGAAGGAGGT

Gapdh, glyceraldehyde 3-phosphate dehydrogenase; *cdh2*, N-cadherin; *Vcam-1*, vascular cell adhesion molecule-1; *Angpt1*, angiopoietin-1; *Thpo*, thrombopoietin.

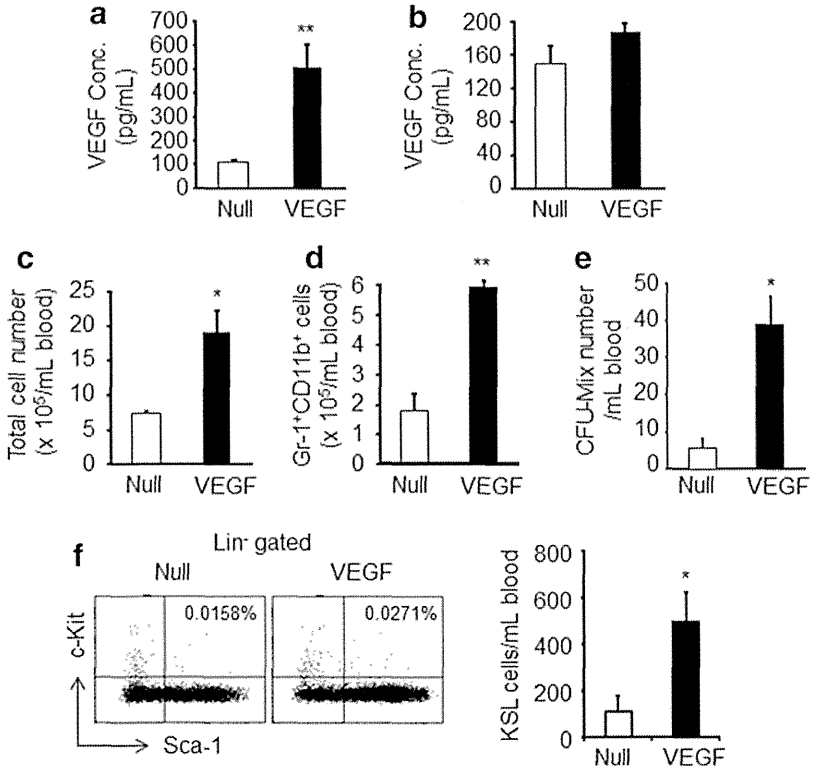

FIG. 1. Effect of vascular endothelial growth factor (VEGF) on the number of myeloid cells and hematopoietic stem/progenitor cells (HSPCs) in peripheral blood. **(a, b)** Mice were intravenously injected with adenovirus (Ad)-Null (Null) or Ad-VEGF (VEGF). Five days later, the concentration of plasma **(a)** and bone marrow (BM) **(b)** VEGF levels was determined by enzyme linked immunosorbent assay (ELISA). Data are expressed as mean ± standard deviation (SD) ($n=4$). **(c)** The number of total peripheral blood mononuclear cells (PBMCs) was counted on day 5 after administration of each Ad vector. **(d)** The percentage of Gr-1$^+$CD11b$^+$ myeloid cells was determined by flow cytometric analysis, and the absolute number was then normalized to the total PBMC number. Data are expressed as mean ± SD ($n=4$). **(e)** The number of colony forming unit (CFU)-Mix/CFU-granulocyte, erythroid, macrophage, megakaryocyte (GEMM) a multipotent hematopoietic progenitor cells, in PBMCs was determined by a standard colony assay. The colony number was normalized to the total PBMC number. **(f)** A representative analysis of the c-Kit$^+$Sca-1$^+$Lineage$^-$(KSL) subset in the blood is shown (*left*). The proportion of cKit$^+$Sca-1$^+$ cells in the lineage-negative (Lin$^-$) population is indicated in the dot blot. The number of KSL cells in the blood was normalized to the total cell number (*right*). Data are expressed as mean ± SD ($n=4$). *$P<0.05$, **$P<0.01$ as compared with Null.

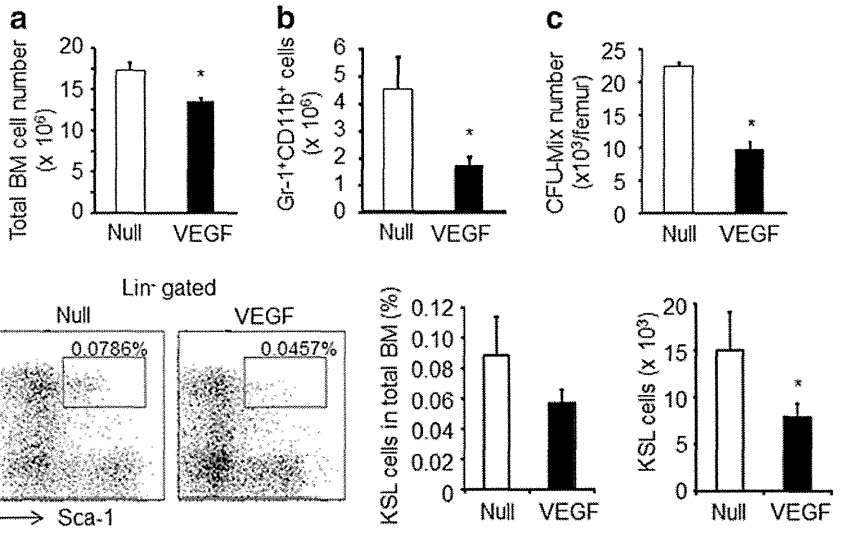

FIG. 2. Plasma elevation of VEGF leads to a decrease in the myeloid cells and HSPCs in the BM. **(a)** The number of total BM cells was counted on day 5 after Ad-Null or Ad-VEGF injection. **(b)** The number of Gr-1$^+$CD11b$^+$ cells in the BM was determined by flow cytometric analysis. **(c)** The number of CFU-Mix/CFU-GEMM in the BM was determined by a colony assay. The colony number was normalized to the total BM cell number. **(d)** A representative analysis of the KSL subset in the BM after administration of Ad-Null or Ad-VEGF is shown (*left*). The proportion of KSL cells in the total BM is indicated in the dot blot. Frequencies (*middle*) and absolute numbers (*right*) of KSL cells in the BM were calculated. Data are expressed as mean ± SD ($n=5$). *$P<0.05$ as compared with Null.

in the reduction in both the frequency and the absolute number of KSL cells in BM (Fig. 2d). Thus, these data suggest that VEGF exerts a physiological effect on the various types of cells within the BM.

Unchanged level of CXCL12 after VEGF overexpression

To examine the mechanisms of BM cell mobilization by VEGF treatment, we analyzed the expression levels of genes associated with HSC maintenance in the BM [*N-cadherin* (*cdh2*), *vascular cell adhesion molecule-1* (*Vcam-1*), *angiopoietin-1* (*Angpt1*), and *thrombopoietin* (*Thpo*)]. The expression levels of these genes in BM nonhematopoietic cells were modestly downregulated after Ad-VEGF injection (Fig. 3a). We next measured the CXCL12 levels in Ad-VEGF-injected mice. Chemokine CXCL12 is an indispensable factor for the maintenance and retention of HSPCs in the BM [5,24]. Previous studies showed that the BM CXCL12 levels were reduced by the injection of mobilization-inducing factors, such as G-CSF and stem cell factor (SCF) [10,25]. We also found that the CXCL12 levels were markedly reduced in the BM, but not the plasma, of Ad-G-CSF-injected mice (Fig. 3b). However, there was almost no difference in the BM CXCL12 levels between Ad-VEGF-injected mice and Ad-Null-injected mice (Fig. 3b). Therefore, these data indicate that VEGF would alter the BM microenvironment, probably by a different mechanism from other mobilization factors.

Reduction of MPCs in the BM after Ad-VEGF injection

Recent studies have demonstrated that MPCs play a pivotal role in HSPC maintenance in the BM [4,6–8]. Therefore, we examined the disposition of MPCs in the BM after Ad-VEGF administration. Flow cytometric analysis of the enzymatically dissociated BM cells revealed that Ad-VEGF overexpression led to a significant reduction of $CD45^-Ter119^-CD31^-Alcam^-Sca\text{-}1^+$ cells, which are reported to be MPCs [21,26] (Fig. 4a). In addition, the percentage of other MPC populations, such as $CD45^-Ter119^-PDGFR\alpha^+Sca\text{-}1^+$ cells [27] and $CD45^-Lineage^-CD31^-CD51^+Sca\text{-}1^+$ cells [28], in the BM of Ad-VEGF-injected mice was also lower than those of Ad-Null-injected mice (Fig. 4b, c). These data clearly showed the decreased number of phenotypically identified MPCs in the BM after injection of Ad-VEGF.

Next, to investigate whether functional MPCs in the BM were reduced in Ad-VEGF-injected mice, we performed a CFU-F assay and homing assay. Consistent with the above data, we observed decreased CFU-F numbers in the BM in Ad-VEGF-injected mice (Fig. 4d). For homing studies, Ad-Null- or Ad-VEGF-injected mice were used as the recipient mice. Donor BM cells derived from GFP transgenic mice were intravenously injected into nonirradiated recipient mice, and the frequency of GFP-expressing cells in the recipient BM was then estimated by flow cytometry. The results showed that the homing activity of GFP-expressing cells was partially inhibited in Ad-VEGF-treated recipient mice (Fig. 4e). Thus, the decreased homing efficiency of donor HSPCs in Ad-VEGF-injected mice suggests the decreased number of niche cells in the BM. Taken together, our findings indicate that overexpression of VEGF in mice leads to a reduction of phenotypic and functional MPCs in the BM.

VEGF stimulates the migration of MPCs

We next examined the mechanisms of the reduction of MPCs in the BM after VEGF overexpression. In vitro-expanded primary mouse BM stromal cells (mBMSCs), including MPCs, showed slight expression of Flt-1 (VEGFR1), but not Flk-1 (VEGFR2), on the cellular surface (Fig. 5a). We speculated that MPCs might egress from the BM in response to the plasma level of VEGF, because there was almost no change in the BM VEGF levels in Ad-VEGF-injected mice (Fig. 1b). We performed an in vitro migration assay and found a dose-dependent chemoattractive effect of VEGF on mBMSCs (Fig. 5b), suggesting the possibility that a decreased number of BM MPCs in Ad-VEGF-injected mice would result from the mobilization of MPCs to the peripheral tissue in response to an elevation of plasma VEGF.

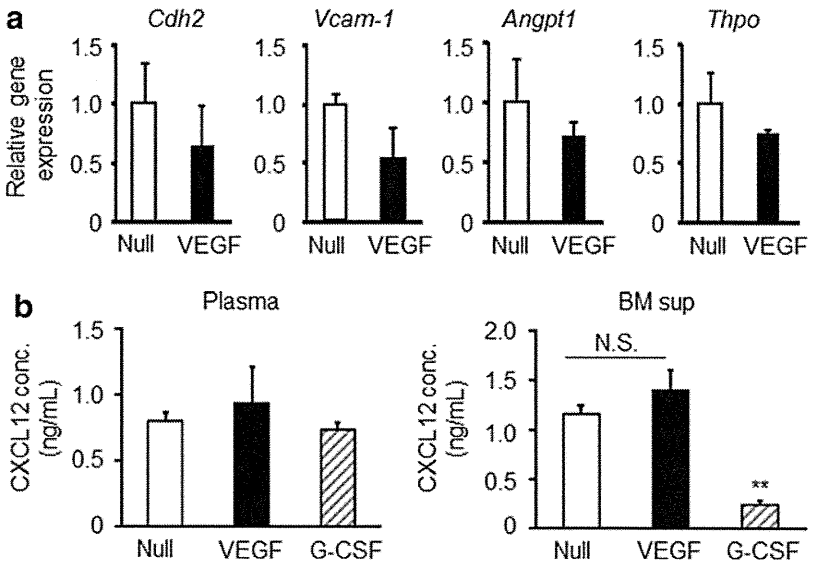

FIG. 3. Expression of HSPC maintenance factor genes after Ad-VEGF administration. **(a)** Expression levels of cadherin2 (Cdh2), vascular cell adhesion molecule-1 (Vcam-1), angiopoietin-1 (Angpt1), and thrombopoietin (Thpo) in nonhematopoietic cells ($CD45^-Ter119^-$ cells) were measured by quantitative polymerase chain reaction analysis. Data are expressed as mean ± SD ($n=3$). **(b)** The plasma and BM supernatants of mice injected with Ad-Null, Ad-VEGF, or Ad-GCSF were collected. The levels of CXC chemokine ligand 12 (CXCL12) in the plasma (*left*) and the BM supernatant (*right*) were measured by ELISA. $^{**}P<0.01$ as compared with Null. N.S. stands for not significant.

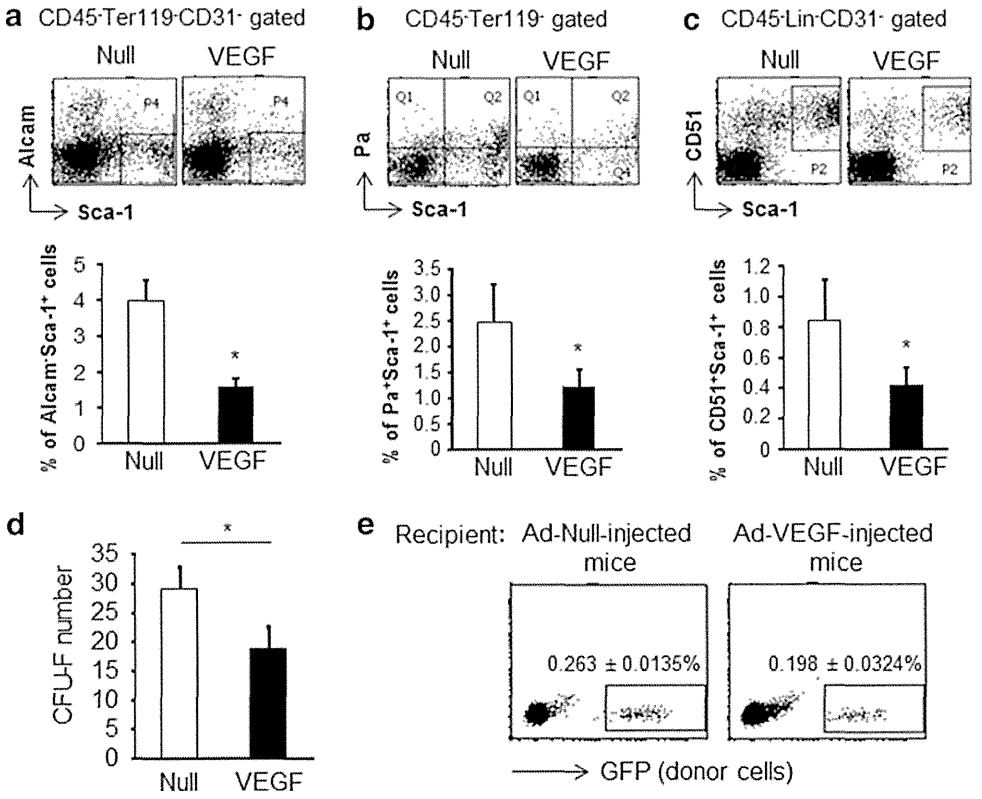

FIG. 4. The number of mesenchymal progenitor cells (MPCs) in the BM is decreased following Ad-VEGF injection. **(a–c)** After BM stromal cells were collected from bone by treatment with collagenase, the proportion of MPC populations [$CD45^-Ter119^-CD31^-Alcam^-Sca\text{-}1^+$ MPCs **(a)**, $CD45^-Ter119^-$ $PDGFRa^+$ (Pa^+) $Sca\text{-}1^+$ MPCs **(b)**, or $Lin^-CD45^-CD31^-CD51^+Sca\text{-}1^+$ MPCs **(c)**] in the BM was determined by flow cytometry. Data are expressed as mean ± SD ($n=5$). **(d)** A colony-forming unit-fibroblast (CFU-F) assay was performed using $CD45^-Ter119^-$ BM cells. The number of CFU-Fs was counted using a microscope after staining with the Giemsa solution. Data are expressed as mean ± SD ($n=3$). **(e)** Homing assay. After injection of Ad-Null or Ad-VEGF into mice, green fluorescent protein (GFP) transgenic mice-derived BM cells (donor cells) were transplanted into Ad vector-administrated mice. The percentage of donor cells (GFP-expressing cells) in the BM of Ad-Null- or Ad-VEGF-injected mice was analyzed by flow cytometry at 16 h after BM transplantation. The percentage of donor cells in the BM is indicated in the dot blot. Data are expressed as mean ± SD ($n=5$). $^*P<0.05$ as compared with Null.

Discussion

Recent studies have clearly reported that the HSPC numbers in the BM are significantly decreased by conditional deletion of MPCs, including nestin-expressing stromal cells [4] and CXCL12-abundant reticular cells [5]. It is of note that deletion of MPCs led to the increased number of HSPCs in the spleen, demonstrating the mobilization of HSPCs from BM to peripheral tissues [4]. Therefore, maintenance and retention of HSPCs in the BM would

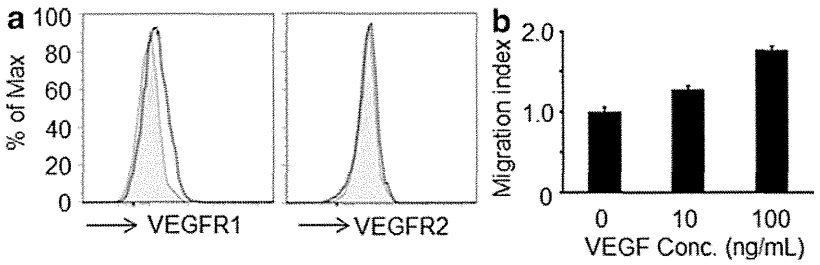

FIG. 5. VEGF enhances the migration capacity of MPCs. BM-derived stromal cells were collected and propagated in a tissue culture dish. **(a)** Expression levels of VEGF receptors, VEGFR1 (*left*) and VEGFR2 (*right*), in the cells was determined by flow cytometry. Staining profiles of specific mAb (*dotted lines*) and an isotype-matched control mAb (*gray area*) are shown. **(b)** BM stromal cells were exposed to various doses of recombinant VEGF. Cells that had migrated toward the VEGF (*lower chamber*) by passing through a membrane filter were counted by microscopy after staining with the Giemsa solution. Data are expressed as mean ± SD ($n=3$).

considerably be dependent on the number of MPCs [4,5]. In the present study, we examined the effect of VEGF on the disposition of BM HSPCs and MPCs in mice. Our main finding was that VEGF overexpression in mice resulted in a reduction of not only HSPCs but also MPCs in the BM. We also found that VEGF could promote the migration of mBMSCs in vitro. The data described here suggest that, as in the case of HSPCs, MPCs would also be mobilized to the peripheral tissues in response to an elevation of plasma VEGF levels, and a reduced number of BM MPCs by VEGF would lead to HSPC egress from the BM, because MPCs would function as niche cells in the BM.

It is well known that BM CXCL12 levels are down-regulated following G-CSF administration and thereby induce an egress of HSPCs [25,29]. Christopher et al. previously showed the reduced BM CXCL12 levels after administration of other mobilization factors, such as SCF and Flt3-ligand [10]. In addition to their mobilization-inducing effects, these factors also impact the number of stem and progenitor cells in the BM. For instance, it has been reported that the number of HSPCs and MPCs in the BM was significantly increased after G-CSF administration [30,31]. Unlike in the case of G-CSF and other mobilization factors, however, VEGF had almost no effect on BM CXCL12 levels (Fig. 3b). Furthermore, systemic VEGF expression resulted in a significant reduction in the number of HSPCs (KSL cells and CFU-Mix) in the BM (Fig. 2). The number of MPCs in the BM was also reduced in Ad-VEGF-injected mice (Fig. 4). Therefore, these data strongly indicate that VEGF would induce HSPC mobilization by altering the BM environment through different mechanisms from G-CSF. Notably, a recent study showed that HSPCs could be mobilized from the BM into the circulation by administration of a prostagrandin E_2 (PGE_2) inhibitor, and this effect was independent of CXCL12-CXCR4 signaling [32]. A nucleotide sugar, uridine diphosphate (UDP)-glucose, has also been shown to mobilize subsets of HSPCs functionally distinct from those mobilized by G-CSF, suggesting that UDP-glucose-induced HSPC mobilization would be mediated, at least in part, by different mechanisms from G-CSF [33]. Thus, it would be of interest to examine whether VEGF could influence the levels of BM PGE_2 and/or plasma UDP glucose.

The expression levels of HSC maintenance genes (*Cdh2*, *Vcam-1*, *Angpt1*, and *Thpo*) in BM nonhematopoietic cells were decreased in Ad-VEGF-injected mice (Fig. 3a). This would be due to the reduction in the number of MPCs in the BM after Ad-VEGF injection (Fig. 4). However, we have no idea why BM CXCL12 levels were not changed in Ad-VEGF-injected mice, because MPCs abundantly produce CXCL12 [7,8]. A detailed investigation would be required to clarify the regulation of CXCL12 expression in niche cells, including MPCs, endosteal osteoblasts, and endothelial cells.

We observed enhanced in vitro migration activities of mBMSCs by VEGF, suggesting the possibility that MPCs in the BM would be mobilized to the peripheral tissue in response to the plasma VEGF concentration. However, at present, we did not detect the CFU-F in the blood in Ad-VEGF-injected mice (data not shown). MPCs are known to be rare cells even in the BM, representing ~ 1 in 10,000–100,000 total nucleated cells [34], and it is therefore possible that the frequency of MPCs in the blood was too low to detect under our experimental conditions. Alternatively, it is also possible that VEGF overexpression in mice might lead to the homing of MPCs to organs, such as the liver, because transgene expression in the liver was extremely high following systemic Ad vector injection [35]. Therefore, it might be necessary to investigate whether or not the frequency and the number of MPCs are changed in tissues or organs other than the peripheral blood.

Recently, Liu et al. showed that MPCs could be mobilized to the peripheral tissue when rats were exposed to hypoxic conditions, and this hypoxia-induced MPC mobilization was caused by the elevation of plasma CXCL12 levels and BM VEGF levels [36]. Under our conditions, however, plasma CXCL12 levels and the BM VEGF levels in Ad-VEGF-injected mice were almost equal to those in Ad-Null-injected mice (Figs. 1b and 3b), suggesting that the mechanisms of decreased number of BM MPCs in Ad-VEGF-injected mice would be different from those of hypoxia-induced MPC mobilization.

Consistent with previous reports [15], we confirmed the HSPC mobilization from BM into the circulation by VEGF overexpression using an Ad vector system (Fig. 1). On the other hand, a previous report showed that administration of a recombinant VEGF protein into mice failed to induce the HSPC mobilization [37]. In our Ad vector systems, plasma VEGF levels were maintained at 400–600 ng/mL on day 3–5 after single intravenous injection. Although we do not know the VEGF levels in the plasma under their experimental protocols, plasma VEGF levels might not be sufficient for HSPC egress from the BM, because exogenous VEGF levels in the plasma were rapidly decreased after administration of a recombinant VEGF protein [23]. Therefore, this difference would be partly due to the difference in the plasma VEGF levels, and we concluded that an Ad vector system would be an appropriate one to estimate the in vivo physiological action of VEGF.

In summary, our results showed that plasma VEGF levels could regulate the distribution of BM HSPCs and MPCs, probably by a mechanism distinct from that of other mobilization factors, and we suggest that a reduction in the number of MPCs in the BM would be one of the mechanisms involved in VEGF-induced HSPC mobilization. Although further investigation of the BM environment will be needed to uncover the VEGF-mediated HSPC mobilization, our findings obtained in this study provide a novel insight into the mechanisms of HSPC mobilization and would be helpful in the development of new clinical mobilizing agents.

Acknowledgments

This work was supported by grants from the Ministry of Health, Labour, and Welfare of Japan, and by the Sasakawa Scientific Research Grant from the Japan Science Society.

Author Disclosure Statement

The authors have no financial conflict of interests.

References

1. Calvi LM, GB Adams, KW Weibrecht, JM Weber, DP Olson, MC Knight, RP Martin, E Schipani, P Divieti, et al.

(2003). Osteoblastic cells regulate the haematopoietic stem cell niche. Nature 425:841–846.
2. Zhang J, C Niu, L Ye, H Huang, X He, WG Tong, J Ross, J Haug, T Johnson, et al. (2003). Identification of the haematopoietic stem cell niche and control of the niche size. Nature 425:836–841.
3. Arai F, A Hirao, M Ohmura, H Sato, S Matsuoka, K Takubo, K Ito, GY Koh and T Suda. (2004). Tie2/angiopoietin-1 signaling regulates hematopoietic stem cell quiescence in the bone marrow niche. Cell 118:149–161.
4. Mendez-Ferrer S, TV Michurina, F Ferraro, AR Mazloom, BD Macarthur, SA Lira, DT Scadden, A Ma'ayan, GN Enikolopov and PS Frenette. (2010). Mesenchymal and haematopoietic stem cells form a unique bone marrow niche. Nature 466:829–834.
5. Omatsu Y, T Sugiyama, H Kohara, G Kondoh, N Fujii, K Kohno and T Nagasawa. (2010). The essential functions of adipo-osteogenic progenitors as the hematopoietic stem and progenitor cell niche. Immunity 33:387–399.
6. Ding L, TL Saunders, G Enikolopov and SJ Morrison. (2012). Endothelial and perivascular cells maintain haematopoietic stem cells. Nature 481:457–462.
7. Ding L and SJ Morrison. (2013). Haematopoietic stem cells and early lymphoid progenitors occupy distinct bone marrow niches. Nature 495:231–235.
8. Greenbaum A, YM Hsu, RB Day, LG Schuettpelz, MJ Christopher, JN Borgerding, T Nagasawa and DC Link. (2013). CXCL12 in early mesenchymal progenitors is required for haematopoietic stem-cell maintenance. Nature 495:227–230.
9. Mendez-Ferrer S, D Lucas, M Battista and PS Frenette. (2008). Haematopoietic stem cell release is regulated by circadian oscillations. Nature 452:442–447.
10. Christopher MJ, F Liu, MJ Hilton, F Long and DC Link. (2009). Suppression of CXCL12 production by bone marrow osteoblasts is a common and critical pathway for cytokine-induced mobilization. Blood 114:1331–1339.
11. Carmeliet P, V Ferreira, G Breier, S Pollefeyt, L Kieckens, M Gertsenstein, M Fahrig, A Vandenhoeck, K Harpal, et al. (1996). Abnormal blood vessel development and lethality in embryos lacking a single VEGF allele. Nature 380:435–439.
12. Ferrara N, K Carver-Moore, H Chen, M Dowd, L Lu, KS O'Shea, L Powell-Braxton, KJ Hillan and MW Moore. (1996). Heterozygous embryonic lethality induced by targeted inactivation of the VEGF gene. Nature 380:439–442.
13. Gerber HP, AK Malik, GP Solar, D Sherman, XH Liang, G Meng, K Hong, JC Marsters and N Ferrara. (2002). VEGF regulates haematopoietic stem cell survival by an internal autocrine loop mechanism. Nature 417:954–958.
14. Chan CK, CC Chen, CA Luppen, JB Kim, AT DeBoer, K Wei, JA Helms, CJ Kuo, DL Kraft and IL Weissman. (2009). Endochondral ossification is required for haematopoietic stem-cell niche formation. Nature 457:490–494.
15. Hattori K, S Dias, B Heissig, NR Hackett, D Lyden, M Tateno, DJ Hicklin, Z Zhu, L Witte, et al. (2001). Vascular endothelial growth factor and angiopoietin-1 stimulate postnatal hematopoiesis by recruitment of vasculogenic and hematopoietic stem cells. J Exp Med 193:1005–1014.
16. Mizuguchi H and MA Kay. (1998). Efficient construction of a recombinant adenovirus vector by an improved *in vitro* ligation method. Hum Gene Ther 9:2577–2583.
17. Mizuguchi H and MA Kay. (1999). A simple method for constructing E1- and E1/E4-deleted recombinant adenoviral vectors. Hum Gene Ther 10:2013–2017.
18. Xu ZL, H Mizuguchi, A Ishii-Watabe, E Uchida, T Mayumi and T Hayakawa. (2001). Optimization of transcriptional regulatory elements for constructing plasmid vectors. Gene 272:149–156.
19. Sakurai H, K Tashiro, K Kawabata, T Yamaguchi, F Sakurai, S Nakagawa, H Mizuguchi. (2008). Adenoviral expression of suppressor of cytokine signaling-1 reduces adenovirus vector-induced innate immune responses. J Immunol 180: 4931–4938.
20. Koizumi N, H Mizuguchi, N Utoguchi, Y Watanabe and T Hayakawa. (2003). Generation of fiber-modified adenovirus vectors containing heterologous peptides in both the HI loop and C terminus of the fiber knob. J Gene Med 5:267–276.
21. Nakamura Y, F Arai, H Iwasaki, K Hosokawa, I Kobayashi, Y Gomei, Y Matsumoto, H Yoshihara and T Suda. (2010). Isolation and characterization of endosteal niche cell populations that regulate hematopoietic stem cells. Blood 116:1422–1432.
22. Okabe M, M Ikawa, K Kominami, T Nakanishi and Y Nishimune. (1997). 'Green mice' as a source of ubiquitous green cells. FEBS Lett 407:313–319.
23. Gabrilovich D, T Ishida, T Oyama, S Ran, V Kravtsov, S Nadaf and DP Carbone. (1998). Vascular endothelial growth factor inhibits the development of dendritic cells and dramatically affects the differentiation of multiple hematopoietic lineages *in vivo*. Blood 92:4150–4166.
24. Sugiyama T, H Kohara, M Noda and T Nagasawa. (2006). Maintenance of the hematopoietic stem cell pool by CXCL12-CXCR4 chemokine signaling in bone marrow stromal cell niches. Immunity 25:977–988.
25. Petit I, M Szyper-Kravitz, A Nagler, M Lahav, A Peled, L Habler, T Ponomaryov, RS Taichman, F Arenzana-Seisdedos, et al. (2002). G-CSF induces stem cell mobilization by decreasing bone marrow SDF-1 and up-regulating CXCR4. Nat Immunol 3:687–694.
26. Ikushima YM, F Arai, K Hosokawa, H Toyama, K Takubo, T Furuyashiki, S Narumiya and T Suda. (2013). Prostaglandin E(2) regulates murine hematopoietic stem/progenitor cells directly via EP4 receptor and indirectly through mesenchymal progenitor cells. Blood 121:1995–2007.
27. Morikawa S, Y Mabuchi, Y Kubota, Y Nagai, K Niibe, E Hiratsu, S Suzuki, C Miyauchi-Hara, N Nagoshi, et al. (2009). Prospective identification, isolation, and systemic transplantation of multipotent mesenchymal stem cells in murine bone marrow. J Exp Med 206:2483–2496.
28. Winkler IG, NA Sims, AR Pettit, V Barbier, B Nowlan, F Helwani, IJ Poulton, N van Rooijen, KA Alexander, LJ Raggatt and JP Levesque. (2010). Bone marrow macrophages maintain hematopoietic stem cell (HSC) niches and their depletion mobilizes HSCs. Blood 116:4815–4828.
29. Levesque JP, J Hendy, Y Takamatsu, PJ Simmons and LJ Bendall. (2003). Disruption of the CXCR4/CXCL12 chemotactic interaction during hematopoietic stem cell mobilization induced by GCSF or cyclophosphamide. J Clin Invest 111:187–196.
30. Brouard N, R Driessen, B Short and PJ Simmons. (2010). G-CSF increases mesenchymal precursor cell numbers in the bone marrow via an indirect mechanism involving osteoclast-mediated bone resorption. Stem Cell Res 5:65–75.
31. Grassinger J, B Williams, GH Olsen, DN Haylock and SK Nilsson. (2012). Granulocyte colony stimulating factor

expands hematopoietic stem cells within the central but not endosteal bone marrow region. Cytokine 58:218–225.
32. Hoggatt J, KS Mohammad, P Singh, AF Hoggatt, BR Chitteti, JM Speth, P Hu, BA Poteat, KN Stilger, et al. (2013). Differential stem- and progenitor-cell trafficking by prostaglandin E2. Nature 495:365–369.
33. Kook S, J Cho, SB Lee and BC Lee. (2013). The nucleotide sugar UDP-glucose mobilizes long-term repopulating primitive hematopoietic cells. J Clin Invest 123:3420–3435.
34. Chamberlain G, J Fox, B Ashton and J Middleton. (2007). Concise review: mesenchymal stem cells: their phenotype, differentiation capacity, immunological features, and potential for homing. Stem Cells 25:2739–2749.
35. Koizumi N, T Yamaguchi, K Kawabata, F Sakurai, T Sasaki, Y Watanabe, T Hayakawa and H Mizuguchi. (2007). Fiber-modified adenovirus vectors decrease liver toxicity through reduced IL-6 production. J Immunol 178:1767–1773.
36. Liu L, Q Yu, J Lin, X Lai, W Cao, K Du, Y Wang, K Wu, Y Hu, et al. (2011). Hypoxia-inducible factor-1alpha is essential for hypoxia-induced mesenchymal stem cell mobilization into the peripheral blood. Stem Cells Dev 20:1961–1971.
37. Pitchford SC, RC Furze, CP Jones, AM Wengner and SM Rankin. (2009). Differential mobilization of subsets of progenitor cells from the bone marrow. Cell Stem Cell 4:62–72.

Address correspondence to:
Dr. Kenji Kawabata
Laboratory of Stem Cell Regulation
National Institute of Biomedical Innovation
7-6-8, Saito-Asagi
Ibaraki, Osaka 567-0085
Japan

E-mail: kawabata@nibio.go.jp

Received for publication September 27, 2013
Accepted after revision December 16, 2013
Prepublished on Liebert Instant Online December 17, 2013

Neuroscience Letters 590 (2015) 126–131

Contents lists available at ScienceDirect

Neuroscience Letters

journal homepage: www.elsevier.com/locate/neulet

Research article

An inhibitory pathway controlling the gating mechanism of the mouse lateral amygdala revealed by voltage-sensitive dye imaging

Tomomi Fujieda[a,b], Noriko Koganezawa[b], Yoshinori Ide[a], Tomoaki Shirao[b], Yuko Sekino[a,b,*]

[a] Division of Pharmacology, National Institute of Health Sciences, 1-18-1 Kamiyoga, Setagaya-ku, Tokyo 158-8501, Japan
[b] Department of Neurobiology and Behavior, Gunma University Graduate School of Medicine, 3-39-22 Showa-machi, Maebashi, Gunma 371-8511, Japan

HIGHLIGHTS

- EC stimulation induces large and long-lasting hyperpolarizing signals in the La.
- This hyperpolarization is analyzed by VSD imaging spatially and temporally.
- We identify an inhibitory pathway toward the La via the m-ITC.

ARTICLE INFO

Article history:
Received 14 January 2015
Received in revised form 28 January 2015
Accepted 29 January 2015
Available online 31 January 2015

Keywords:
External capsule
GABAergic neurons
Hyperpolarization
Lateral amygdala
Medial intercalated cluster
Voltage-sensitive dye imaging

ABSTRACT

The lateral amygdala nucleus (La) is known as a gateway for emotional learning that interfaces sensory inputs from the cortex and the thalamus. In the La, inhibitory GABAergic inputs control the strength of sensory inputs and interfere with the initial step of the acquisition of fear memory. In the present study, we investigated the spatial and temporal patterns of the inhibitory responses in mouse La using voltage-sensitive dye imaging. Stimulating the external capsule (EC) induced large and long-lasting hyperpolarizing signals in the La. We focused on these hyperpolarizing signals, revealing the origins of the inhibitory inputs by means of surgical cuts on the possible afferent pathways with four patterns. Isolating the medial branch of EC (ECmed), but not the lateral branch of EC (EClat), from the La strongly suppressed the induction of the hyperpolarization. Interestingly, isolating the ECmed from the caudate putamen did not suppress the hyperpolarization, while the surgical cut of the ECmed fiber tract moderately suppressed it. Glutamatergic antagonists completely suppressed the hyperpolarizing signals induced by the stimulation of EC. When directly stimulating the dorsal, middle or ventral part of the ECmed fiber tract in the presence of glutamatergic antagonists, only the stimulation in the middle part of the ECmed caused hyperpolarization. These data indicate that the GABAergic neurons in the medial intercalated cluster (m-ITC), which receive glutamatergic excitatory input from the ECmed fiber tract, send inhibitory afferents to the La. This pathway might have inhibitory effects on the acquisition of fear memory.

1. Introduction

The amygdala is an important brain structure for emotional behavior and learning [13]. Fear conditioning is a widely-used experimental model to examine emotional and learning processing in animal brains. The lateral amygdala nucleus (La) is known as a gateway for emotional learning that interfaces sensory inputs from the cortex and the thalamus [14]. Inhibitory circuits are known to control the amygdala's functions, such as acquisition, expression, and extinction of conditioned fear [6,21,22]. Inhibitory inputs to the La control the strength of sensory inputs and interfere with the initial step of the acquisition of fear memory. Two groups of GABAergic neurons in the amygdala are known: local interneurons that are scattered within the local neuropil [17], and intercalated cells organized in clusters (intercalated clusters) surrounding the amygdala complex [15,16,18,20,23,24]. Although inhibitory inputs to the individual principal neurons in the amygdala have been analyzed electrophysiologically [4,26,31,37,38], how sensory inputs

* Corresponding author at: Division of Pharmacology, National Institute of Health Sciences, 1-18-1 Kamiyoga, Setagaya-ku, Tokyo 158-8501, Japan.
Tel.: +81 3 3700 9692; fax: +81 3 3700 1452.
E-mail address: yukos@nihs.go.jp (Y. Sekino).

http://dx.doi.org/10.1016/j.neulet.2015.01.079

induce inhibitory responses in the La, and how inhibitory responses propagate in the La, are still unclear because of the technical limitations of patch clamp recording.

Optical imaging techniques overcome these limitations to investigating propagations in a wide range of neuronal interactions, and have been applied in the study of excitatory circuits of several brain regions [7,9,11,12,29,33,34]. In this study, using optical imaging techniques, we investigate neuronal activities in the La, focusing particularly on inhibitory responses. To identify the origins of the inhibitory inputs, we perform various patterns of knife-cut operations of the possible afferent pathways evoking hyperpolarization in the La. In addition, we investigate the effects of glutamatergic antagonists on the inhibitory responses in the La, and show an inhibitory pathway from the medial intercalated cluster (m-ITC) to the La.

2. Materials and methods

2.1. Slice preparation and staining procedure

The experimental protocol was reviewed and approved by the National Institute of Health Sciences (NIHS) in Japan, following the guidelines in the National Research Council's 'Guide for the Care and Use of Laboratory Animals'. All experiments were approved by the NIHS' ethics committee. Male mice (C57BL/6J, 7–22 weeks old, Japan SLC, Inc., Japan) were deeply anesthetized with halothane and quickly decapitated. Coronal slices containing the amygdala complex (400 μm) were prepared using a vibrating microtome (Campden Instruments Ltd., Loughborough, UK) in ice-cold artificial cerebrospinal fluid (ACSF). The ACSF was composed of the following (in mM): 119 NaCl, 2.5 KCl, 1.3 $MgSO_4$, 2.5 $CaCl_2$, 1.0 NaH_2PO_4, 26.2 $NaHCO_3$, and 11.0 glucose; this was oxygenated with a mixture gas of 95% O_2 and 5% CO_2 (pH 7.4). The slices were immediately soaked in the oxygenated ACSF containing a voltage-sensitive dye (VSD), di-4-ANEPPS (50 μM, Invitrogen Molecular Probes Inc., Oregon, USA) for 10 s, and then transferred to a filter that absorbed the staining solution and subsequently to another filter that absorbed the normal ACSF for at least an hour before the experiment.

2.2. Experimental apparatus for VSD imaging

An epi-illumination macro zoom fluorescence microscopy (MVX-10 MacroView, Olympus, Japan), a LED light source with a 530 nm center wavelength (LEX2-Green, Brainvision Inc., Tokyo, Japan), a dichroic mirror (560 nm), an emission filter (BP 575–625 nm), and a CMOS imaging device (MiCAM ULTIMA-L, Brainvision Inc., Tokyo) were used for VSD imaging.

The decrease and increase in the fluorescent intensity from the preparation corresponded to the membrane depolarization and hyperpolarization, respectively. Each data acquisition consisted of 1024 images of consecutive frames (1.0 ms/frame). A coaxial needle electrode (TF203-047, Unique Medical Co. Ltd., Tokyo, Japan) was placed on the external capsule (EC). Electrical stimuli with 200-μs duration at various intensities from 15 to 90 μA were delivered at the 100th frame of each acquisition. To analyze the effects of deafferentation on the induction of the hyperpolarization, the stimulus intensity was adjusted to make the peak value of depolarization equal before and after the surgical cut. Methods to calculate optical signals and present images were described in previous papers [11,29,32].

2.3. Surgical cuts of afferent connections to the La

After recording the optical signals at various stimulation intensities, we performed knife-cut operations on the pathways assumed to be involved in the induction of the hyperpolarization in the La. Four afferent pathways to the La were cut under the macro scope observation, as follows: the La was isolated by the longitudinal cut from: (i) the lateral branch of the EC, (ii) the medial branch of the EC and (iii) the CPu, and by (iv) the transverse cut of ECmed at the dorsal part. For the sham operations, the slices remained intact but the same procedure was carried out. After the surgical cuts, the slices were stored in the recovery chamber at room temperature (at least 1 h).

2.4. Excitation and inhibition values

Images from the 251st–300th frames were stacked and averaged to determine regions of interest (ROIs), which were circles of 8 pixels in diameter. Two ROIs were defined for each experiment. One of the ROIs had the maximal hyperpolarization value in the center spot. The other was adjacent to the first, which had an adequately large hyperpolarization value within the region. For the after-operation analysis, the ROIs were centered on the spots that had the same distances from the position of the stimulating electrode and the EC as the before-operation analysis. The averaged optical signals of the two ROIs were used as representative data.

The excitation (E) value was determined as the largest value among all the values from the first to the 15th frame after electrical stimulation. The inhibition (I) value was determined by averaging 50 frames, from the 251st frame to the 300th frame after the electrical stimulation.

2.5. Statistical analysis

We defined the operation index (OI) as follows: $OI = [I/E]_a/[I/E]_b$, where a: after the operation, b: before the operation. The data were presented as mean ± standard error of the mean (SEM). Normality of the data was tested with the Shapiro–Wilk test, and subsequently one-way ANOVA followed by Dunnett's post-hoc test was carried out. In the pharmacological experiments, inhibition value was statistically analyzed using a paired t-test.

3. Results

3.1. Optical signal propagation after the EC stimulation

The anatomical nomenclatures related to our experiments are shown in Fig. 1A. Each white fiber bundle in the amygdala slice preparation was observed through the macro zoom microscope; thus, the ramifying point of the EC was identified. The La, BLA, and CeA of the amygdala complex were identified in the fluorescent image recorded by the system (Fig. 1B). In Fig. 1C, a typical example of the optical signal propagation is shown in pseudo-color representation. The depolarization started at the stimulation point and spread over the La within 3 ms after the stimulation (0–3 ms). It became stronger in the La and spread over the other regions, the BLA, CPu, and CeA (4–7 ms). Then the depolarization at the dorsal area of the La faded, while growing stronger in the other regions (8–11 ms). Following depolarization, a weak hyperpolarization was first observed in the La; the depolarization remained in the other regions, although it was weakened (12–15 ms). The hyperpolarization grew stronger, and the depolarization in the other regions gradually disappeared (16–19 ms). The hyperpolarization in the La lasted about 600–650 ms (the middle wave in Fig. 1B). The maximal value of the hyperpolarization was observed around 255 ms after the stimulation.

After the hyperpolarization started in the La at the area along the dorsal part of the ECmed (16–19 ms), it spread out in the La during the next 100 ms (20–119 ms), then it spread over the BLA and a narrow part of the CPu along the dorsal part of the ECmed

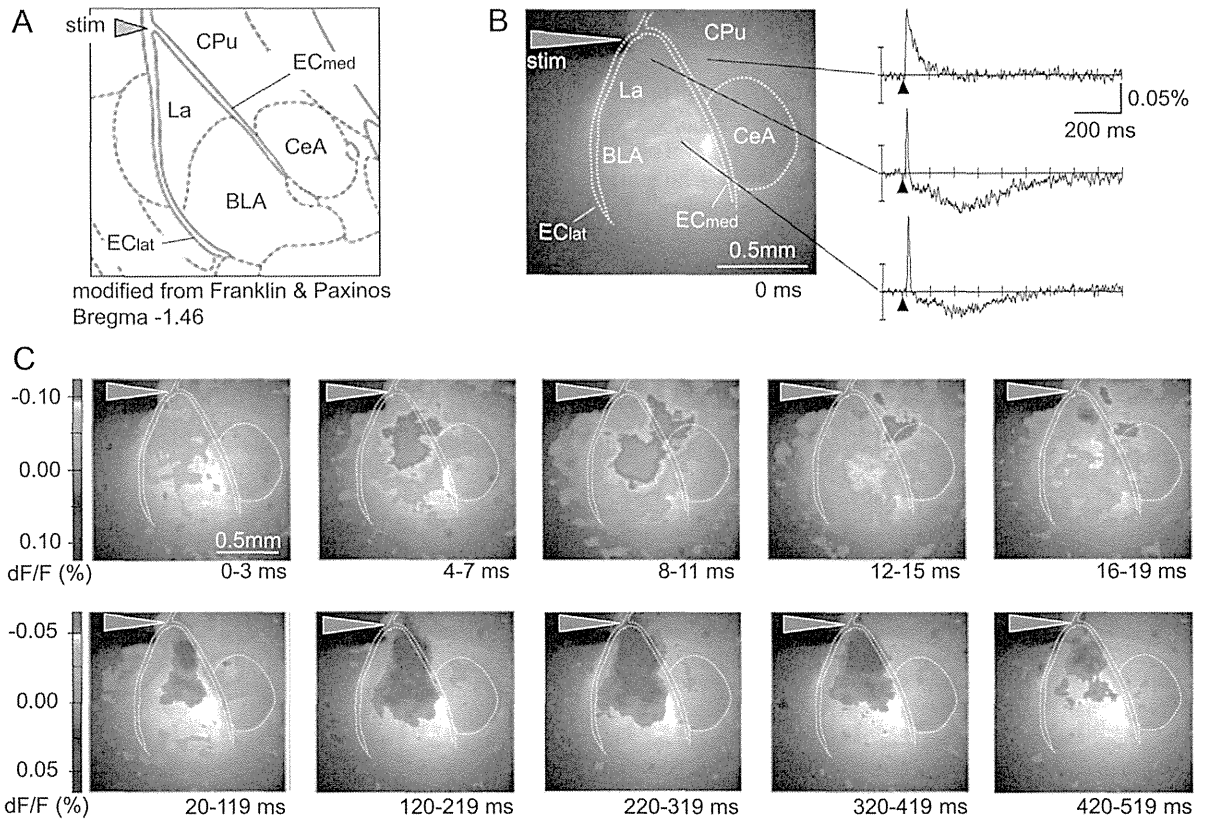

Fig. 1. Optical signal propagation after the EC stimulation.
(A) The modified schematic diagram from the atlas of Franklin and Paxinos (2007) at Bregma −1.46 mm. The arrowhead shows the ramifying point of the external capsule (EC); lateral branch of the external capsule (EClat) and medial branch of the external capsule (ECmed). La – lateral amygdala nucleus; BLA – basolateral amygdala nucleus; CeA – central amygdala nucleus; CPu – caudate putamen. (B) Left, the fluorescence image of VSD-stained coronal slice. Right, a typical example of optical signals in the CPu (in the top wave), La (in the middle wave) and BLA (in the bottom wave). Brown arrowhead, the stimulating site; black arrowhead, the timing of electrical stimulation. (C) Images of optical signal changes produced at the various indicated times after electrical stimulation. In the upper panels, images for 4 frames were stacked to show the spread pattern of depolarization. In the lower panels, images for 100 frames were stacked to show the spread pattern of hyperpolarization.

during the following 100 ms (120–219 ms). The maximal hyperpolarization was observed in the La along the dorsal part of the ECmed from 220 to 319 ms. The strong and long-lasting hyperpolarization was mainly observed in the La (the middle wave in Fig. 1B), while the hyperpolarization in the BLA was weak (the bottom wave). The hyperpolarization was neither observed in the main part of the CPu (the top wave) nor in the CeA, while the depolarization in the CPu lasted longer than in the La and the BLA.

3.2. *Effects of the deafferentation on the optical signals*

To reveal the afferent pathway responsible for evoking the strong and long-lasting hyperpolarization, effects of the various surgical operations were investigated.

Deafferentation from the EClat to the La did not affect the induction of the strong and long-lasting hyperpolarization in the La (Fig 2A), and there was no significant change in the OI value compared with the sham (Fig. 2E), suggesting that the afferent inputs via the EClat are not involved in the hyperpolarization induced in the La. In contrast, deafferentation from the ECmed to the La strongly reduced the hyperpolarization (Fig. 2B). OI values were also significantly reduced (Fig. 2E). These results suggest that the inputs via the ECmed are involved in the hyperpolarization induced in the La.

Next, to investigate the involvement of inputs from the main part of the CPu, we cut off the input from the CPu to the ECmed. In this experiment, the connections between the ECmed and the La remained. The OI values after deafferentation did not significantly change (Fig. 2C and E), suggesting that the inputs from the CPu are not involved in the hyperpolarization induced in the La. For further investigation of the inputs via ECmed, a transverse cut at the dorsal part of the ECmed was carried out. As a result, the hyperpolarization was significantly reduced in the La (Fig. 2D). These data suggest that the fibers running along the ECmed were involved in the induction of hyperpolarization.

3.3. *Effects of glutamatergic antagonists and the source of the inhibition*

Finally, to confirm the details of the inhibitory input source and its properties, the effects of glutamatergic antagonists (6-cyano-7-nitroquinoxaline-2,3-dione (CNQX, 10 μM, TOCRIS), D-(−)-2-amino-5-phosphonopentanoic acid (D-AP5, 50 μM, TOCRIS)) on the inhibitory responses were investigated. The inhibitory responses in the La induced by EC stimulation were statistically significantly reduced after the application of glutamatergic antagonists (Fig. 3A), suggesting that excitatory glutamatergic inputs were involved in the inhibitory response.

We then stimulated several parts along the ECmed in the presence of glutamatergic antagonists (Fig. 3B). Stimulation at the dorsal part of the ECmed did not induce the hyperpolarization (Fig. 3Ba); however, the hyperpolarization could be induced when the middle part of the ECmed was stimulated (Fig. 3Bb). When the electrode moved to the ventral part of the ECmed, weak hyperpolarizing responses were observed (Fig. 3Bc). The magnitude of the hyperpolarization induced by the stimulation at the middle part of the ECmed was statistically significantly larger than that induced by

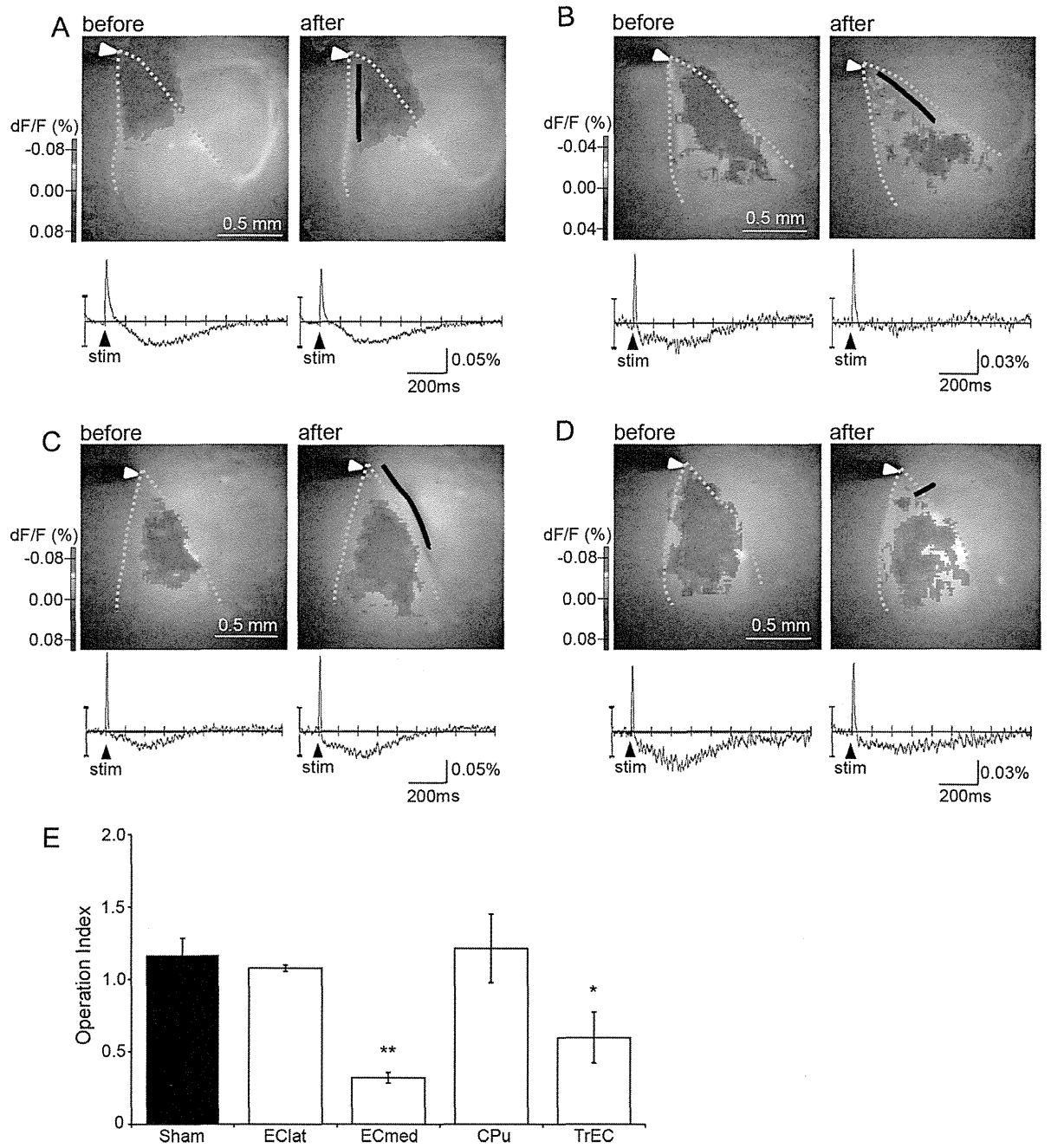

Fig. 2. Effects of deafferentation of the lateral amygdala nucleus on the inhibitory responses.
(A–C) Afferent pathways to the lateral amygdala nucleus were surgically cut from the lateral branch of the external capsule (EClat) in (A), the medial branch (ECmed) in (B), and the caudate putamen (CPu) in (C) to the La was performed, respectively. Black lines, the surgical cut sites; white arrowhead, the stimulating site. The upper images of panels A, B, and C show the spread pattern of hyperpolarization before and after operation. Lower traces, the optical signal traces; black arrowhead, the timing of electrical stimulation. (D) The dorsal part of the ECmed was cut transversely (TrEC). (E) Operation indices (OIs) were quantitatively analyzed among various deafferentations. OIs of ECmed ($n = 6$ slices from 6 mice) and TrEC ($n = 7$ slices from 4 mice) were significantly lower than those of Sham ($n = 5$ slices from 3 mice), EClat ($n = 5$ slices from 4 mice), and CPu ($n = 7$ slices from 4 mice). $^{*}p < 0.05$; $^{**}p < 0.01$.

the stimulation at the other parts (Fig. 3Bd). These results suggest that inhibitory neurons located in the middle part of the ECmed are the main source of the hyperpolarization in the La.

4. Discussion

VSD imaging is a powerful tool to investigate spatial and temporal patterns in the propagation of membrane potential change in the brain tissue. Furthermore, optical signals from the stained slice preparation with VSD are reported to be well-correlated to field EPSPs in vitro [7,8,10,19,25,29,32]. In the amygdala, the signal propagations from the La to the BLA [35,36] and from the La to the CeA have been visualized using VSD imaging [3]. However, these previous studies focused on the propagation of depolarizing signals in the amygdala but not of hyperpolarizing signals.

In the present study, we demonstrated the propagation of the inhibitory responses in the amygdala formation using VSD imaging. The strong and long-lasting hyperpolarization is evoked in the La after the sharp and strong depolarization. In addition, the surgical-cut and the pharmacological experiments indicate that the source of the inhibitory responses is not located in the La or the CPu, but is located in the middle part of the ECmed. According to this

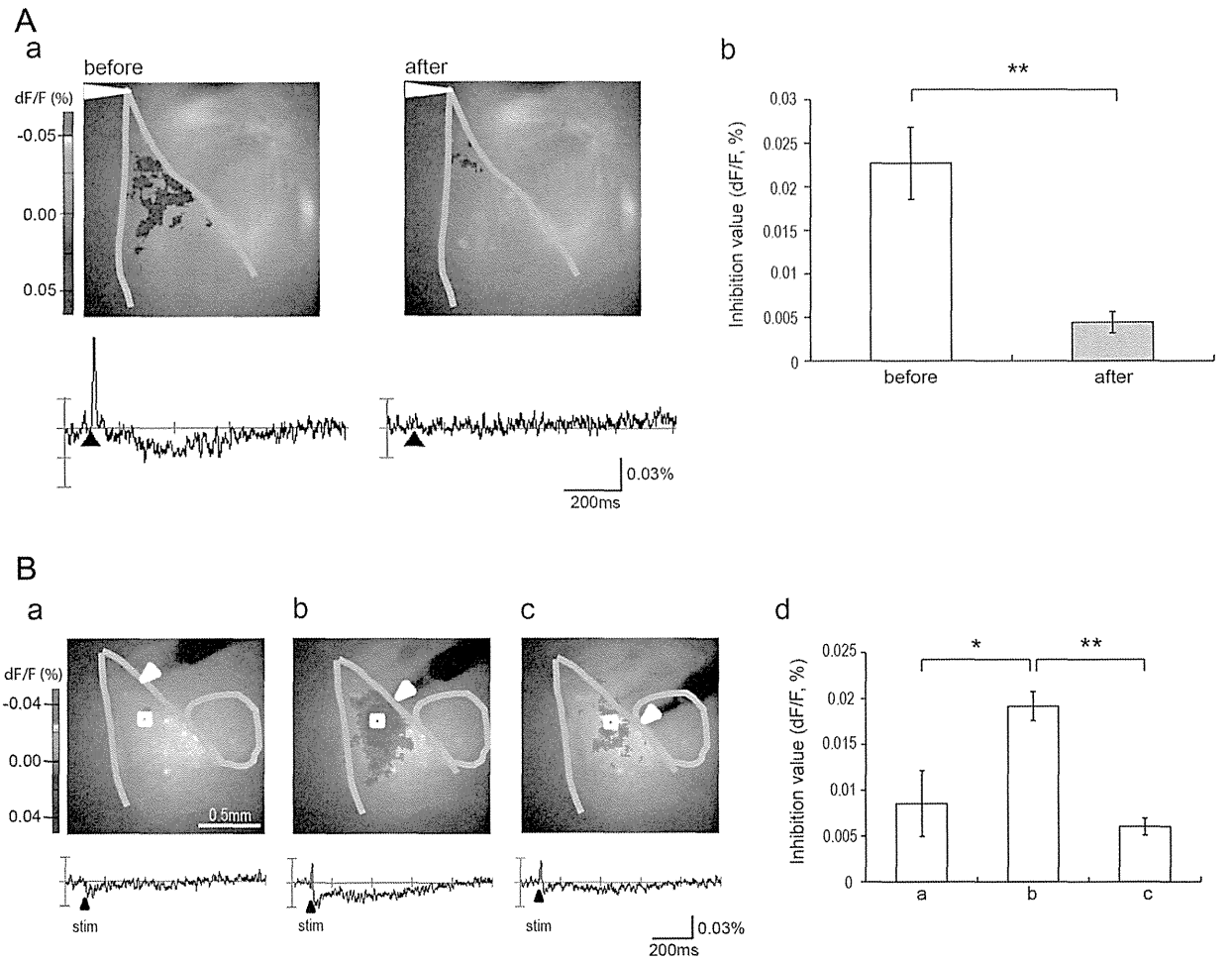

Fig. 3. Effects of glutamatergic antagonists on the inhibitory responses.
(A) The effects of glutamatergic antagonists (CNQX + D-AP5) on the inhibitory response induced by the stimulation of the ramifying point of the external capsule. (Aa) Left and right upper images indicate the spread pattern of hyperpolarization before and after the drug application, respectively. White arrowhead, the stimulating site; lower traces, the optical signal traces; black arrowhead, the timing of electrical stimulation. (Ab) Inhibitory value was statistically compared between before and after CNQX + D-AP5 application ($n = 5$ slices from 5 mice; $^{**}p < 0.01$). (B) The dependence of the stimulus position on inhibitory response of the La in the presence of CNQX + D-AP5. (Ba–c) Upper images indicate the spread pattern of hyperpolarization when the stimulus electrode was at the dorsal, middle, and ventral part of the ECmed, respectively. White arrowhead, the stimulating site; lower traces, the optical signal traces; white squares, the area of which the traces were calculated; black arrowhead, the timing of electrical stimulation. (Bd) Inhibitory value was shown when the stimulus electrode was at the dorsal (a), middle (b), and ventral (c) part of the ECmed ($n = 4$ slices from 4 mice; $^{*}p < 0.05$; $^{**}p < 0.01$).

anatomical location, the source of the inhibitory inputs is likely from the m-ITC in the ECmed [5,18,20,27]. The inhibitory responses were completely eliminated in the presence of the glutamatergic antagonists, indicating that the inhibitory responses are based on the glutamatergic input passing through ECmed. Furthermore, local stimulation of the middle part of the ECmed produces inhibitory responses even in the presence of glutamatergic antagonists, suggesting that GABAergic neurons in the m-ITC are the source of the inhibitory responses of the La. A TrEC cut results in a smaller reduction of the inhibitory responses than an ECmed cut. Because it has been reported that stimulation of the La and the BLA excites the m-ITC neurons [27,28], excitatory glutamatergic inputs to the m-ITC through the La and the BLA might be involved in the inhibitory response in addition to the glutamatergic inputs coming along the ECmed.

In the present study, the contribution of the lateral intercalated clusters located in the EClat was smaller than that of the m-ITC, although the pathway from the lateral intercalated clusters to the BLA has been shown anatomically and electrophysiologically [16,30]. Because the direction of the stimulus electrode used in the present study was from the EClat to the ECmed, resulting in the selective stimulation of the ECmed, the contribution of the lateral intercalated clusters to the inhibitory response in vivo cannot be excluded.

It has been reported that the stimulation of the La and the BLA excites the m-ITC neurons [27,28], resulting in the inhibition of the CeA neurons [2,27]. This pathway is suggested to be involved in the fear extinction mechanism [1], while the inhibitory inputs from m-ITC to La might interfere with the acquisition of fear memory.

In summary, the present study demonstrates the spatial and temporal spread pattern of the inhibitory response in the La after the stimulation of the EC using VSD imaging. Moreover, it is indicated that the inhibitory response is induced via the m-ITC. The pathway from the m-ITC to the La might have inhibitory effects on the acquisition of fear memory.

Acknowledgements

We thank Drs. Miwa and Shimizu for their support. This work was supported by Research Grants from MHLW.

References

[1] T. Amano, C.T. Unal, D. Pare, Synaptic correlates of fear extinction in the amygdala, Nat. Neurosci. 13 (2010) 489–494.
[2] A. Amir, T. Amano, D. Pare, Physiological identification and infralimbic responsiveness of rat intercalated amygdala neurons, J. Neurophysiol. 105 (2011) 3054–3066.
[3] C. Avrabos, S.V. Sotnikov, J. Dine, P.O. Markt, F. Holsboer, R. Landgraf, M. Eder, Real-time imaging of amygdalar network dynamics in vitro reveals a neurophysiological link to behavior in a mouse model of extremes in trait anxiety, J. Neurosci. 33 (2013) 16262–16267.
[4] E.P. Bauer, J.E. LeDoux, Heterosynaptic long-term potentiation of inhibitory interneurons in the lateral amygdala, J. Neurosci. 24 (2004) 9507–9512.
[5] D. Busti, R. Geracitano, N. Whittle, Y. Dalezios, M. Manko, W. Kaufmann, K. Satzler, N. Singewald, M. Capogna, F. Ferraguti, Different fear states engage distinct networks within the intercalated cell clusters of the amygdala, J. Neurosci. 31 (2011) 5131–5144.
[6] I. Ehrlich, Y. Humeau, F. Grenier, S. Ciocchi, C. Herry, A. Luthi, Amygdala inhibitory circuits and the control of fear memory, Neuron 62 (2009) 757–771.
[7] A. Grinvald, L.B. Cohen, S. Lesher, M.B. Boyle, Simultaneous optical monitoring of activity of many neurons in invertebrate ganglia using a 124-element photodiode array, J. Neurophysiol. 45 (1981) 829–840.
[8] A. Grinvald, A. Manker, M. Segal, Visualization of the spread of electrical activity in rat hippocampal slices by voltage-sensitive optical probes, J. Physiol. 333 (1982) 269–291.
[9] T. Iijima, M.P. Witter, M. Ichikawa, T. Tominaga, R. Kajiwara, G. Matsumoto, Entorhinal-hippocampal interactions revealed by real-time imaging, Science 272 (1996) 1176–1179.
[10] W. Jin, R.J. Zhang, J.Y. Wu, Voltage-sensitive dye imaging of population neuronal activity in cortical tissue, J. Neurosci. Methods 115 (2002) 13–27.
[11] M.Z. Kee, J.P. Wuskell, L.M. Loew, G.J. Augustine, Y. Sekino, Imaging activity of neuronal populations with new long-wavelength voltage-sensitive dyes, Brain Cell Biol. 36 (2008) 157–172.
[12] N. Koganezawa, A. Taguchi, T. Tominaga, S. Ohara, K. Tsutsui, M.P. Witter, T. Iijima, Significance of the deep layers of entorhinal cortex for transfer of both perirhinal and amygdala inputs to the hippocampus, Neurosci. Res. 61 (2008) 172–181.
[13] J.E. LeDoux, Emotion circuits in the brain, Annu. Rev. Neurosci. 23 (2000) 155–184.
[14] J.E. LeDoux, P. Cicchetti, A. Xagoraris, L.M. Romanski, The lateral amygdaloid nucleus: sensory interface of the amygdala in fear conditioning, J. Neurosci. 10 (1990) 1062–1069.
[15] D. Marcellino, M. Frankowska, L. Agnati, M. Perez de la Mora, V. Vargas-Barroso, K. Fuxe, J. Larriva-Sahd, Intercalated and paracapsular cell islands of the adult rat amygdala: a combined rapid-Golgi, ultrastructural, and immunohistochemical account, Neuroscience 226 (2012) 324–347.
[16] A. Marowsky, Y. Yanagawa, K. Obata, K.E. Vogt, A specialized subclass of interneurons mediates dopaminergic facilitation of amygdala function, Neuron 48 (2005) 1025–1037.
[17] A.J. McDonald, Neurons of the lateral and basolateral amygdaloid nuclei: a Golgi study in the rat, J. Comp. Neurol. 212 (1982) 293–312.
[18] O.E. Millhouse, The intercalated cells of the amygdala, J. Comp. Neurol. 247 (1986) 246–271.
[19] M. Nakamura, Y. Sekino, T. Manabe, GABAergic interneurons facilitate mossy fiber excitability in the developing hippocampus, J. Neurosci. 27 (2007) 1365–1373.
[20] L. Nitecka, Y. Ben-Ari, Distribution of GABA-like immunoreactivity in the rat amygdaloid complex, J. Comp. Neurol. 266 (1987) 45–55.
[21] H.C. Pape, D. Pare, Plastic synaptic networks of the amygdala for the acquisition, expression, and extinction of conditioned fear, Physiol. Rev. 90 (2010) 419–463.
[22] D. Pare, G.J. Quirk, J.E. Ledoux, New vistas on amygdala networks in conditioned fear, J. Neurophysiol. 92 (2004) 1–9.
[23] D. Pare, Y. Smith, Distribution of GABA immunoreactivity in the amygdaloid complex of the cat, Neuroscience 57 (1993) 1061–1076.
[24] D. Pare, Y. Smith, The intercalated cell masses project to the central and medial nuclei of the amygdala in cats, Neuroscience 57 (1993) 1077–1090.
[25] D. Plenz, A. Aertsen, Current source density profiles of optical recording maps: a new approach to the analysis of spatio-temporal neural activity patterns, Eur. J. Neurosci. 5 (1993) 437–448.
[26] D.G. Rainnie, E.K. Asprodini, P. Shinnick-Gallagher, Inhibitory transmission in the basolateral amygdala, J. Neurophysiol. 66 (1991) 999–1009.
[27] S. Royer, M. Martina, D. Pare, An inhibitory interface gates impulse traffic between the input and output stations of the amygdala, J. Neurosci. 19 (1999) 10575–10583.
[28] S. Royer, M. Martina, D. Pare, Polarized synaptic interactions between intercalated neurons of the amygdala, J. Neurophysiol. 83 (2000) 3509–3518.
[29] Y. Sekino, K. Obata, M. Tanifuji, M. Mizuno, J. Murayama, Delayed signal propagation via CA2 in rat hippocampal slices revealed by optical recording, J. Neurophysiol. 78 (1997) 1662–1668.
[30] Y. Silberman, L. Shi, J.K. Brunso-Bechtold, J.L. Weiner, Distinct mechanisms of ethanol potentiation of local and paracapsular GABAergic synapses in the rat basolateral amygdala, J. Pharmacol. Exp. Ther. 324 (2008) 251–260.
[31] C. Szinyei, T. Heinbockel, J. Montagne, H.C. Pape, Putative cortical and thalamic inputs elicit convergent excitation in a population of GABAergic interneurons of the lateral amygdala, J. Neurosci. 20 (2000) 8909–8915.
[32] T. Tominaga, Y. Tominaga, H. Yamada, G. Matsumoto, M. Ichikawa, Quantification of optical signals with electrophysiological signals in neural activities of Di-4-ANEPPS stained rat hippocampal slices, J. Neurosci. Methods 102 (2000) 11–23.
[33] Y. Tominaga, M. Ichikawa, T. Tominaga, Membrane potential response profiles of CA1 pyramidal cells probed with voltage-sensitive dye optical imaging in rat hippocampal slices reveal the impact of GABA(A)-mediated feed-forward inhibition in signal propagation, Neurosci. Res. 64 (2009) 152–161.
[34] S. Tsuda, M.Z. Kee, C. Cunha, J. Kim, P. Yan, L.M. Loew, G.J. Augustine, Probing the function of neuronal populations: combining micromirror-based optogenetic photostimulation with voltage-sensitive dye imaging, Neurosci. Res. 75 (2013) 76–81.
[35] C. Wang, M.H. Kang-Park, W.A. Wilson, S.D. Moore, Properties of the pathways from the lateral amygdal nucleus to basolateral nucleus and amygdalostriatal transition area, J. Neurophysiol. 87 (2002) 2593–2601.
[36] C. Wang, W.A. Wilson, S.D. Moore, Role of NMDA, non-NMDA, and GABA receptors in signal propagation in the amygdala formation, J. Neurophysiol. 86 (2001) 1422–1429.
[37] A.R. Woodruff, H. Monyer, P. Sah, GABAergic excitation in the basolateral amygdala, J. Neurosci. 26 (2006) 11881–11887.
[38] A.R. Woodruff, P. Sah, Networks of parvalbumin-positive interneurons in the basolateral amygdala, J. Neurosci. 27 (2007) 553–563.

OPEN ACCESS Freely available online

PLOS ONE

Myosin II ATPase Activity Mediates the Long-Term Potentiation-Induced Exodus of Stable F-Actin Bound by Drebrin A from Dendritic Spines

Toshiyuki Mizui[1,3], Yuko Sekino[1,2*¤a], Hiroyuki Yamazaki[1], Yuta Ishizuka[1], Hideto Takahashi[1¤b], Nobuhiko Kojima[1], Masami Kojima[2,3], Tomoaki Shirao[1*]

1 Department of Neurobiology and Behavior, Gunma University Graduate School of Medicine, Maebashi, Gunma, Japan, **2** Core Research for Evolution Science and Technology, Japan Science and Technology Corporation, Kawaguchi, Saitama, Japan, **3** Bio-interface Research Group, Health Research Institute, National Institute of Advanced Industrial Science and Technology (AIST), Ikeda, Osaka, Japan

Abstract

The neuronal actin-binding protein drebrin A forms a stable structure with F-actin in dendritic spines. NMDA receptor activation causes an exodus of F-actin bound by drebrin A (DA-actin) from dendritic spines, suggesting a pivotal role for DA-actin exodus in synaptic plasticity. We quantitatively assessed the extent of DA-actin localization to spines using the spine-dendrite ratio of drebrin A in cultured hippocampal neurons, and found that (1) chemical long-term potentiation (LTP) stimulation induces rapid DA-actin exodus and subsequent DA-actin re-entry in dendritic spines, (2) Ca^{2+} influx through NMDA receptors regulates the exodus and the basal accumulation of DA-actin, and (3) the DA-actin exodus is blocked by myosin II ATPase inhibitor, but is not blocked by myosin light chain kinase (MLCK) or Rho-associated kinase (ROCK) inhibitors. These results indicate that myosin II mediates the interaction between NMDA receptor activation and DA-actin exodus in LTP induction. Furthermore, myosin II seems to be activated by a rapid actin-linked mechanism rather than slow MLC phosphorylation. Thus the myosin-II mediated DA-actin exodus might be an initial event in LTP induction, triggering actin polymerization and spine enlargement.

Citation: Mizui T, Sekino Y, Yamazaki H, Ishizuka Y, Takahashi H, et al. (2014) Myosin II ATPase Activity Mediates the Long-Term Potentiation-Induced Exodus of Stable F-Actin Bound by Drebrin A from Dendritic Spines. PLoS ONE 9(1): e85367. doi:10.1371/journal.pone.0085367

Editor: Makoto Sato, Osaka University Graduate School of Medicine, Japan

Received September 30, 2013; **Accepted** November 25, 2013; **Published** January 22, 2014

Funding: This work was supported by Grants-in-Aid for Scientific Research (16300117, 19200029) and on Priority Areas - Elucidation of neural network function in the brain - from the Ministry of Education, Culture, Sports, Science and Technology of Japan (20021002). The funders had no role in study design, data collection and analysis, decision to publish, or preparation of the manuscript.

Competing Interests: The authors have declared that no competing interests exist.

* E-mail: yukos@nihs.go.jp (YS); tshirao@ gunma-u.ac.jp (TS)

¤a Current address: Division of Pharmacology, National Institute of Health Sciences, Setagaya-ku, Tokyo, Japan
¤b Current address: Institut de recherches cliniques de Montréal (IRCM), Université de Montréal (UdeM), Québec, Canada

Introduction

Drebrin A is a neuron-specific actin-binding protein that is located at the base of dendritic spine heads [1–3]. Drebrin A binding modifies the pitch of actin filaments [4–5] and forms stable F-actin that is resistant to depolymerization by cytochalasin D [6–7]. Mikati *et al* [8] have recently shown that F-actin that is bound by drebrin A (DA-actin) is stable, and the depolymerization of DA-actin is suppressed at both ends of the filaments. In developing neurons, DA-actin is not observed in dynamic dendritic filopodia, but is observed in more stable dendritic spines [9]. Furthermore, DA-actin is suitable for the formation of a stable higher-order F-actin structure (DA-actin complex), because drebrin A has two F-actin-binding domains that can act cooperatively to enable interfilament interactions [10]. Together, it is suggested that DA-actin forms stable structures of F-actin at the base of dendritic spine heads.

Dendritic spines at rest contain a dynamic F-actin pool that shows quick treadmilling, and a stable pool that shows slow treadmilling. The dynamic pool is observed at the tip of the spine head, whereas the stable pool is located at the base of the spine head [11]. The aforementioned stability and localization of DA-actin suggest that DA-actin is a major component of the stable F-actin pool in dendritic spines, whereas F-actin that is not bound by drebrin A (non-DA-actin) is a major component of the dynamic F-actin pool (for review, see Shirao and González-Billault [12]).

We have previously shown that NMDA receptor activation induces the loss of drebrin A from dendritic spines [13]. Because our previous biochemical analyses revealed that most drebrin A in neurons is bound to F-actin (for a review, see Sekino *et al* [14]), we can extrapolate DA-actin localization from drebrin immunostaining images. Furthermore, fluorescence recovery after photobleaching analysis has demonstrated that drebrin A dynamics in spines are far slower than those of monomeric proteins such as monomeric actin [15] and cortactin [16], indicating that drebrin A remains bound to F-actin even when drebrin A dynamically changes its localization [17]. Together, it is suggested that NMDA receptor activation induces the DA-actin exodus from dendritic spines. However, the mechanism by which NMDA receptor activation links to the DA-actin exodus remains to be elucidated.

It has recently been reported that myosin II ATPase activity is necessary for actin reorganization during long-term potentiation (LTP) induction [18]. We have previously shown that myosin II is

contained in the DA-actin complex [19], but the interaction between myosin II and DA-actin is suppressed in the DA-actin complex [20]. The release of the actomyosin interaction leads to the activation of myosin II ATPase, resulting in reorganization of the actin cytoskeleton through severing of F-actin [21]. Therefore, LTP stimulation might disinhibit the suppressed actomyosin interaction, resulting in the activation of myosin II ATPase.

In this study, we quantitatively assessed the extent to which DA-actin localizes to dendritic spines, clarified DA-actin migration in the context of synaptic plasticity and examined whether myosin II mediates the interaction between NMDA receptor activation and DA-actin exodus.

Materials and Methods

All animal experiments were performed with the permission of the Animal Care and Experimentation Committee, Gunma University, Showa Campus (Maebashi, Japan). All efforts were made to minimize animal suffering and reduce the number of animals used in this study.

Reagents

4-aminopyridine (4-AP) and pyruvate were purchased from Sigma (St. Louis, MO, USA). Hexahydro-1-[(5-iodo-1-naphthalenyl) sulfonyl]-1*H*-1,4-diazepine hydrochloride (ML-7) and (*S*)-(+)-2-Methyl-1-[(4-methyl-5-isoquinolinyl)sulfonyl]-hexahydro-1*H*-1,4-diazepine dihydrochloride (H-1152) were purchased from Calbiochem (San Diego, CA, USA). Ethyleneglycol-*bis* (β-aminoethyl)-N,N,N',N'-tetraacetic acid (EGTA) was purchased from Dojin (Kumamoto, Japan). Tetrodotoxin (TTX) was purchased from Wako (Osaka, Japan). D-(−)-2-amino-5-phosphonopentanoic acid (APV), bicuculline, (S)-(−)-blebbistatin, (R)-(+)-blebbistatin, thapsigargin and nifedipine were purchased from Tocris (Ellisville, MO, USA).

Hippocampal neuron cultures

Timed pregnant Wistar rats (Charles River Laboratories Inc., Yokohama, Japan) were deeply anesthetized with diethyl ether and sacrificed by decapitation. Hippocampi were dissected from the fetuses at embryonic day 18. The hippocampal cells were prepared by trypsinization and mechanical dissociation according to previously described methods [9]. Briefly, the cell suspensions were plated at a density of 5000 cells/cm^2 on coverslips coated with poly-L-lysine (Sigma). Cells were incubated in Minimum Essential Medium (MEM; Invitrogen, San Diego, CA, USA) supplemented with 10% fetal bovine serum (Invitrogen), 0.6% glucose (Wako), and 1 mM pyruvate (Sigma). After the cells achieved attachment, the coverslips were transferred to a culture dish containing a glial monolayer and maintained in normal medium consisting of serum-free MEM, 2% B27 supplement (Invitrogen), 0.6% glucose, and 1 mM sodium pyruvate at 35.8°C in a humidified incubator with 5% CO_2 for 21 days *in vitro* (DIV). Cytosine β-D-arabinofuranoside (10 μM; Sigma) was added to the cultures at 4 DIV to inhibit glial proliferation.

Pharmacological treatments

The chemical LTP (cLTP) stimulation solution used in this study was Mg^{2+}-free Tyrode's solution supplemented with 200 μM glycine, 20 μM bicuculline, 1 μM strychnine and 0.5 μM TTX [22]. For cLTP induction, the neurons were preincubated in cLTP stimulation solution without 200 μM glycine for 20 min, and then stimulated with glycine for the indicated amount of time.

For blocker experiments, the neurons were preincubated in medium supplemented with blocker for 30 min and then stimulated with cLTP stimulation solution or 100 μM glutamate in the presence of each blocker for the indicated amount of time. For the stimulation studies with 90 mM potassium chloride, the neurons were preincubated in Tyrode's solution (119 mM NaCl, 2.5 mM KCl, 2 mM $CaCl_2$, 2 mM $MgSO_4$, 25 mM HEPES [pH 7.4], and 30 mM glucose).

Immunocytochemistry

After three weeks *in vitro*, cells were fixed in 4% paraformaldehyde with 0.1% glutaraldehyde in phosphate-buffered saline (PBS; pH 7.4) at 4°C for 10 min. The fixed cells were permeabilized with 0.1% Triton X-100 in PBS for 3 min and then incubated in blocking solution (3% bovine serum albumin in PBS) for 1 h, followed by an overnight incubation with primary antibodies at 4°C. A monoclonal antibody against drebrin (clone M2F6, hybridoma supernatant [23]) was used at a 1:1 dilution. F-actin was detected with rhodamine-conjugated phalloidin (Molecular Probes, Eugene, OR, USA). After being washed with PBS for 30 min, the cells were incubated for 1 h at room temperature with secondary antibodies. Anti-mouse IgG antibodies conjugated to fluorescein (Cappel, West Chester, PA, USA) were used to detect the monoclonal antibodies against drebrin. After being washed with PBS, the cells were mounted on glass slides with Perma Fluor mounting medium (Thermo Shandon, Pittsburgh, PA, USA).

Labeling of surface GluR1 was performed according to previous reports [22,24] with minor modifications. Briefly, after the cLTP stimulation, surface GluR1 was labeled in live neurons by 30 min incubation with a rabbit polyclonal antibody against the N-terminus of the GluR1 subunit (PC246, 1:15 dilution in glial conditioned media; Calbiochem). After washout of the antibody with Hank's balanced salt solution, the neurons were fixed in 2% PFA for 20 min at 4°C without permeabilization. The surface receptors were visualized using a fluorescein-conjugated goat anti-rabbit secondary antibody (Cappel).

Fluorescence microscopy

All fluorescence images were obtained on a Zeiss Axioplan 2 microscope (Zeiss, Jena, Germany) equipped with a Cool Snap fx CCD camera (Photometrics, Tucson, AZ, USA), a 63×, 1.4 numerical aperture objective lens (Zeiss), and MetaMorph software (Universal Imaging, West Chester, PA, USA). A filter set (86000 Sedat Quad; Chroma, Brattleboro, VT, USA) was mounted in the excitation and emission filter wheels (Ludl Electronic Products, Hawthorne, NY, USA) of the microscope. All data were collected at 1300×1030 resolution at 12 bits/pixel. A single pixel in the image corresponded to a 106 nm^2 area in the specimen plane. The images used for comparison in this study were collected under identical conditions. The captured fluorescence images were analyzed using the MetaMorph program. The GFP, rhodamine, and Cy5 signals were obtained through filters for FITC, Cy3, and Cy5, respectively. We found no fluorescence leakage of these signals through the other filters. The images presented in this study were prepared using Adobe Photoshop software (Adobe Systems, San Jose, CA, USA).

Plasmids and Transfection

Construction of the green fluorescent protein-tagged drebrin A (GFP-DA) has been described previously [25]. At 7 DIV, the hippocampal neurons were transfected with plasmids using a calcium phosphate coprecipitation protocol [26]. Two weeks after transfection, the transfected neurons were analyzed using time-lapse imaging.

Time-lapse imaging

Live time-lapse imaging was performed at 35.8°C on a Zeiss inverted microscope stage using a temperature-controlled chamber with continuous perfusion, as described previously [7]. Briefly, the cell cultures were mounted in a chamber containing Mg^{2+}-free Tyrode's solution supplemented with 20 μM bicuculline, 1 μM strychnine and 0.5 μM TTX. The chamber was maintained and perfused with the same solution. The perfusing solution (1 ml/min) was switched between the control and cLTP stimulation medium using a hydraulic two-way valve switch with a dead space of 3.5 ml between the switch and the bath. Thus, the test medium would reach the chamber 210 sec after flipping the switch (data not shown). The time-lapse images were acquired at 10 sec intervals for 20 min using MetaMorph software.

Image analysis and quantification

All quantifications were performed by an observer who was blind to the experimental conditions, and the morphological analysis was performed using the MetaMorph software. Each experiment was repeated at least three times with independent neuronal preparations.

For quantification, spiny neurons with pyramidal morphology were selected from at least three separate cultures. In our hippocampal cultures, we have previously shown that pyramidal neurons are multipolar cells with a large soma and multiple thick dendritic processes [27]. Therefore, we considered that these multipolar cells were hippocampal pyramidal neurons. Although the hippocampal culture also contains a variety of interneurons, they are comparatively few in number and most are morphologically distinguishable in culture [28].

To measure the surface cluster density of GluR1, the number of GluR1 clusters was measured according to previously described methods [24,29] with minor modifications. Briefly, the surface GluR1 signals were thresholded with intensity at two-fold the dendritic background to mark surface clusters of GluR1 using MetaMorph software. The surface clusters were selected using the 'regions' tool and analyzed using the 'integrated morphometry' feature. Next, the length of the analyzed region on a dendrite was measured. The density of surface GluR1 clusters were obtained by dividing the number of surface GluR1 clusters within a selected dendritic region by the length of the dendrite (50–100 μm total dendritic length per neuron).

Calculation of the spine-dendrite ratio

The spine-dendrite ratio (SDR) used in this study was the average fluorescence signal of the molecule of interest in a dendritic spine head divided by the average fluorescence signal of that molecule in the dendritic shaft at the foot of the spine. To measure the SDR, a single dendrite located between the cell soma and the second branch point (30–80 μm total dendritic length per neuron) was selected from each neuron. The dendritic spines and the shaft in the selected region were outlined on the F-actin fluorescence images, and circles (0.26 μm^2) were drawn at dendritic spine heads and at the foot of the spine in a dendritic shaft, using the 'ellipse region' tool of the MetaMorph software (Fig. 1A). Next, the average fluorescence intensity in each circle (calculated from the fluorescence signal intensity values) was measured using the 'region measurements' tool in the MetaMorph software. The number of spines measured were between 25 and 80 per neuron. The average SDR of spines per neuron was then calculated. The drebrin immunostaining and rhodamine-phalloidin signal intensity values were used to calculate the drebrin and F-actin SDRs, respectively.

Statistical analysis

The statistical analysis included a one-way ANOVA followed by a post hoc Scheffe's test. A Student's t test was performed for comparisons between control and drug-treated neurons. All data were presented as mean ± s.e.m. A p value of <0.01 was considered significant. The statistical analysis was performed using Microsoft Excel (Redmond, WA, USA).

Results

Quantitative assessment of DA-actin in dendritic spines

We used the spine-dendrite ratio (SDR) of drebrin immunostaining intensity to monitor the amounts of DA-actin in dendritic spines. We used the SDR of rhodamine-phalloidin staining intensity to assess the amount of total F-actin. The SDR used in this study is the average fluorescence signal of the molecule of interest in a dendritic spine head divided by the average fluorescence signal of that molecule in the dendritic shaft at the foot of the spine (Fig. 1A). The drebrin SDR of control cultured hippocampal neurons at 21 days *in vitro* (DIV) was 1.65 ± 0.03 ($n = 170$ cells), whereas the actin SDR was 1.67 ± 0.02 ($n = 170$ cells; Fig. 1B), demonstrating that both DA-actin and total F-actin accumulate more in the dendritic spines than the parent dendrites.

Chemical LTP stimulation induces a transient DA-actin exodus

Stimulation with chemical LTP (cLTP) solution for 3 min induced a significant increase in the glutamate receptor subunit 1 (GluR1) cluster density 30 min after treatment (Fig. 2). This increase was inhibited with 50 μM 2-amino-5-phosphonopentanoate (APV), an NMDA receptor blocker (Fig. 2). These data are consistent with an earlier study showing facilitated insertion of α-amino-3-hydroxy-5-methyl-4-isoxazolepropionic acid (AMPA) receptors during cLTP [22].

We examined whether cLTP stimulation would induce DA-actin to exit dendritic spines. At 5 min after cLTP stimulation, the intensity of drebrin immunostaining in dendritic spines was weak, but after 30 min the intensity was similar to that in untreated cells (Fig. 3A). Quantitative analysis showed that both drebrin and actin SDRs were significantly lower at 5 min but recovered after 30 min (Fig. 3B).

To analyze the time course of the DA-actin migration, we transfected a GFP-drebrin A-expressing vector into cultured hippocampal neurons and performed time-lapse imaging. The GFP-drebrin A SDR was transiently decreased following cLTP stimulation, similar to that of the native drebrin A (Fig. 3C). The GFP-drebrin A SDR began to decrease immediately after the neurons were exposed to cLTP solution (arrow in Fig. 3D) and then further declined throughout the period of stimulation. When the stimulation medium was switched back to control medium, the SDR began to rise and returned to the control level in 11 min after the completion of cLTP stimulation (Fig. 3D).

cLTP-induced DA-actin exodus is dependent on myosin II activity

Neurons were pretreated with 100 μM (S)-(−)-blebbistatin (aBL, the active form of blebbistatin), a myosin II ATPase blocker, for 30 min [30]. In the presence of aBL, cLTP stimulation did not affect the localization of either drebrin or actin in dendritic spines (photomicrographs in Fig. 4), and failed to decrease the drebrin and actin SDRs ($n = 30$ cells; $p = 0.37$ for drebrin SDR at 5 min, $p = 0.34$ for actin SDR; Student's *t* test; graphs in Fig. 4). This result indicates that myosin II activity is involved in the DA-actin

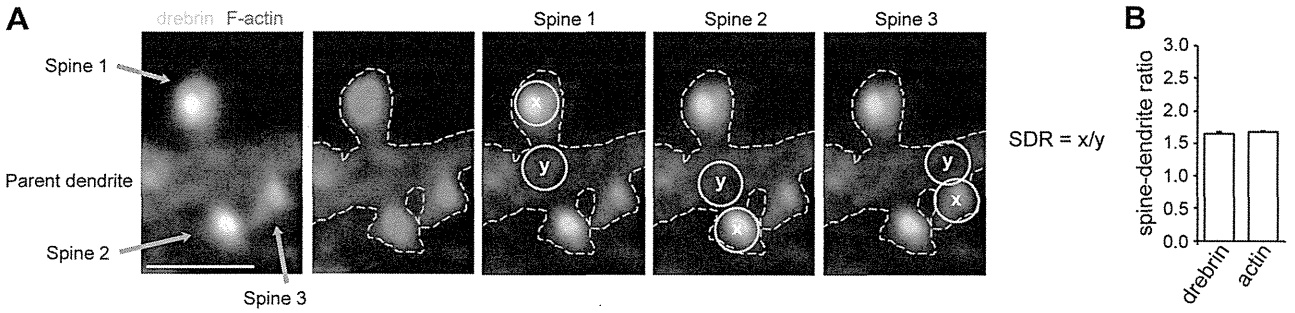

Figure 1. Spine-dendrite ratios of drebrin and actin. (**A**) Fluorescence images of drebrin (green) and F-actin (red) in control hippocampal neurons. The dendritic spines and the parent dendrite in the selected region were outlined on the F-actin fluorescence images (white dotted lines). Scale bar, 2 μm. Circles (0.26 μm^2, yellow) were drawn at the spine head and at the parent dendrite, and the average fluorescence intensities within the circles were measured. The SDR of each spine was obtained by dividing the average intensity of the dendritic spine by that of the parent dendrite. (**B**) The SDR per neuron was obtained as the average SDR of the spines. Bar graph shows the drebrin and actin SDRs of 21-DIV hippocampal neurons (n = 170 cells). Error bars represent s.e.m.
doi:10.1371/journal.pone.0085367.g001

exodus. The inactive form of blebbistatin (iBL) was used as a control. In the presence of iBL, cLTP stimulation significantly decreased the drebrin and actin SDRs.

Various kinds of stimulation induce DA-actin exodus

We stimulated cultured hippocampal neurons with 100 μM glutamate for 10 min, and fixed them immediately after the stimulation. This treatment induced the loss of drebrin and F-actin from dendritic spines (photomicrographs in Fig. 5A). On the other hand, it did not affect the density of spines or presynaptic terminals (Fig. S1). Quantitative analyses showed significant reductions in both the drebrin and actin SDRs (graphs in Fig. 5A).

We then examined whether other kinds of excitatory stimulation affect DA-actin localization. Increased spontaneous firing rates resulting from a 30-minute application of 50 μM bicuculline, a $GABA_A$ receptor blocker, combined with 500 μM 4-aminopyridine, a potassium channel blocker [31], induced a loss of drebrin and F-actin from dendritic spines (photomicrographs in Fig. 5B). A similar decrease was induced by membrane depolarization resulting from a 5-minute application of 90 mM KCl (photomicrographs in Fig. 5C). Quantitative analyses showed that both treatments significantly decreased the drebrin and actin SDRs (graphs in Fig. 5B, C). These data indicate that in addition to cLTP stimulation, various kinds of excitatory stimulation induce a DA-actin exodus.

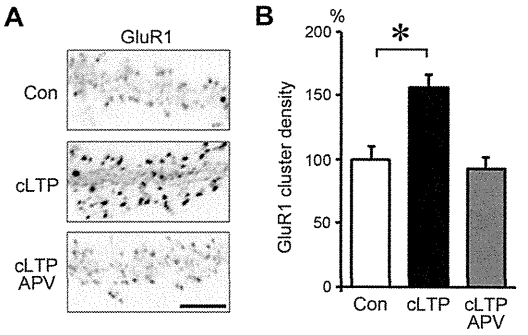

Figure 2. Increase in surface GluR1 immunostaining after chemical LTP (cLTP) stimulation. Neurons (21 DIV) were stimulated with buffer containing 0 μM Mg^{2+}, 200 μM glycine, 20 μM bicuculline, 1 μM strychnine and 0.5 μM TTX (cLTP stimulation) for 3 min. (**A**) Surface GluR1 was labeled before the stimulation (top panel; Con) or 30 min after the stimulation (middle panel; cLTP). Note that cLTP stimulation remarkably increased surface GluR1 immunostaining. The increase was completely blocked by APV (bottom panel; cLTP APV). Scale bar, 7 μm. (**B**) Quantitative analysis of surface GluR1 cluster density along dendrites. Data are expressed as percentages relative to the average of control neurons. In the absence of APV, cLTP stimulation significantly increased the density of surface GluR1 clusters (n = 21 cells; $p<0.01$, Scheffe's test). In contrast, in the presence of APV, no increase in surface GluR1 cluster density was observed following cLTP stimulation (cLTP APV). Error bars represent s.e.m.
doi:10.1371/journal.pone.0085367.g002

Localization of DA-actin and non-DA-actin is differentially regulated by glutamate receptor subtypes

We examined the effect of APV on DA-actin and total F-actin levels in dendritic spines. In the presence of 50 μM APV, drebrin and F-actin were localized at dendritic spines, and this localization was not changed by glutamate stimulation (photomicrographs in Fig. 6A).

However, quantitative analysis showed that the treatment of neurons with APV for 30 min resulted in significant increases in both drebrin and actin SDRs relative to controls. Interestingly, the increase in actin SDR (ca. 130% of control) is smaller than that of the drebrin SDR (ca. 180% of control; Fig. 6A). This indicates that NMDA receptor activity affects the basal accumulation level of DA-actin in dendritic spines more strongly than that of non-DA-actin. If non-DA-actin is not at all affected by APV, the above data suggest that about 40% of total F-actin is DA-actin. Furthermore, in the presence of APV, glutamate stimulation failed to decrease the drebrin SDR but did decrease the actin SDR (Fig. 6A). The disparity between drebrin and actin SDRs indicates that glutamate stimulation decreases the non-DA-actin even in the presence of APV.

Together, it is suggested that the NMDA receptor mediates both the glutamate-induced DA-actin exodus and the basal accumulation of DA-actin in dendritic spines, whereas glutamate receptor subtypes other than the NMDA receptor, such as AMPA or metabotropic glutamate receptors, mediate the non-DA-actin exodus.

The DA-actin exodus is not regulated by voltage-dependent Ca^{2+} channels or intracellular Ca^{2+} stores

Because NMDA receptor activation leads to Ca^{2+} influx, we examined whether Ca^{2+} regulates the DA-actin distribution. When extracellular Ca^{2+} was chelated by 20 mM ethylene glycol tetraacetic acid (EGTA), the localization pattern of drebrin and F-

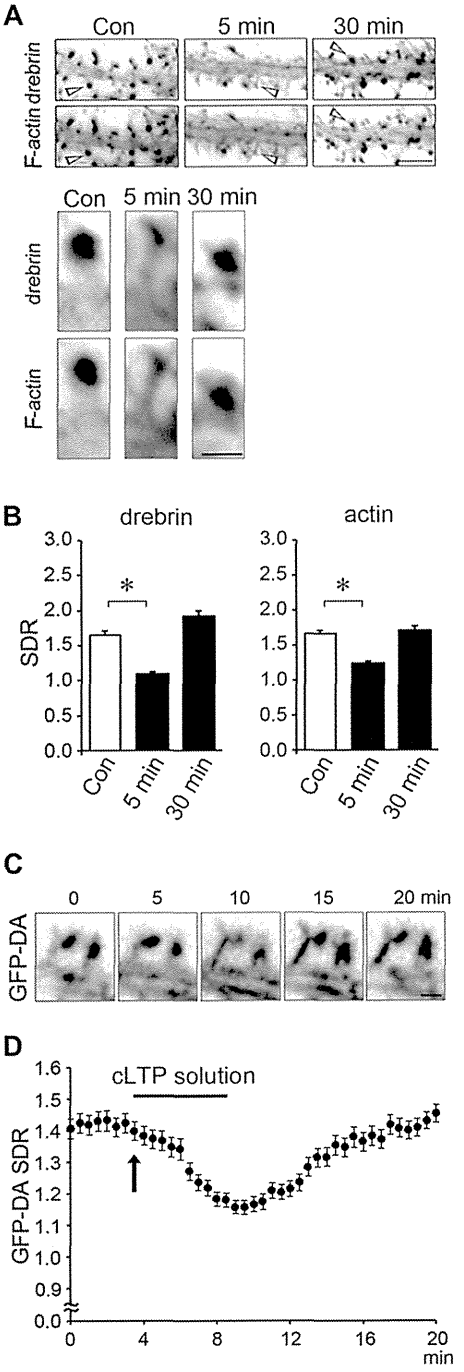

Figure 3. Chemical LTP (cLTP) stimulation induces the exodus and re-entry of DA-actin. (**A**) Neurons (21 DIV) were stimulated with a buffer containing 0 μM Mg^{2+}, 200 μM glycine, 20 μM bicuculline, 1 μM strychnine and 0.5 μM TTX (cLTP stimulation) for 3 min and then fixed 5 or 30 min after stimulation. The fixed cells were double-labeled for drebrin and F-actin. Scale bars, 5 μm and 1 μm in upper and lower panels, respectively. The lower panels show the higher-magnification images of the spines (indicated by arrow heads) in the upper panels. (**B**) Bar graphs represent the spine-dendrite ratios (SDRs) for drebrin and actin. cLTP stimulation significantly decreased the drebrin and actin SDRs at 5 min (n = 30 cells; $p<0.01$, Student's *t* test). Error bars represent s.e.m. (**C, D**) We transfected 7-DIV neurons with a GFP-drebrin A (GFP-DA)-expressing vector and performed time-lapse imaging at 21 DIV. Scale bar, 1 μm. (C) shows the GFP-DA images at 0, 5, 10, 15 and 20 min after the start of the time-lapse recording. The neurons were stimulated with cLTP solution from 3.5 min (indicated by an arrow) to 8.5 min. In (D), closed circles represent data obtained at 30-sec intervals. Error bars represent s.e.m. (n = 7 neurons). The GFP-DA SDR began to decrease soon after cLTP stimulation. When the stimulation was stopped, the GFP-DA SDR began to increase and recovered to control levels within 10 min.
doi:10.1371/journal.pone.0085367.g003

actin in dendritic spines was similar for both with and without glutamate stimulation (photomicrographs in Fig. 6B). However, quantitative analysis showed that EGTA treatment significantly increased both the drebrin and actin SDRs compared with control neurons. Following the extracellular Ca^{2+} chelation, glutamate stimulation failed to induce decreases in drebrin and actin SDRs (n = 30 cells; p = 0.88 for drebrin SDR, p = 0.84 for actin SDR; Student's *t* test; graphs in Fig. 6B). These data indicate that Ca^{2+} influx is involved in the changes in both DA-actin and non-DA-actin distribution.

Inhibition of L-type voltage-dependent Ca^{2+} channels with 20 μM nifedipine did not block glutamate-induced changes in drebrin and F-actin localization (photomicrographs in Fig. 6C). Quantitative analysis also showed that nifedipine treatment did not inhibit the glutamate-induced decreases in drebrin and actin SDRs. However, in the absence of glutamate stimulation, nifedipine treatment significantly increased the drebrin and actin SDR levels, similar to the results obtained with APV and EGTA treatments (graphs in Fig. 6C). This indicates that voltage-dependent Ca^{2+} channels regulate the accumulation of DA-actin in dendritic spines, but do not regulate the DA-actin exodus. However, we cannot exclude the possibility that the increase of the basal SDR is due to inhibition of voltage-dependent Ca^{2+} channels in the presynaptic terminus.

Inhibition of Ca^{2+} release from intracellular stores with 1 μM thapsigargin [32] did not block glutamate-induced changes in drebrin and F-actin localization (photomicrographs in Fig. 6D). Quantitative analysis showed that thapsigargin neither increased the drebrin and actin SDRs (n = 30 cells; p = 0.99 for drebrin SDR, p = 0.50 for actin SDR; Student's *t* test) nor blocked the glutamate-induced decreases in drebrin and actin SDRs (n = 30 cells: $p<0.01$, Scheffe's test; graphs in Fig. 6D).

Together, these data indicate that DA-actin exodus is regulated by NMDA receptors, but not by voltage-dependent Ca^{2+} channels. On the other hand, the basal accumulation of DA-actin in dendritic spines is regulated by both NMDA receptors and voltage-dependent Ca^{2+} channels. Ca^{2+} release from intracellular stores is not involved in either the DA-actin exodus or the basal accumulation of DA-actin.

Glutamate-induced DA-actin exodus is also dependent on myosin II ATPase activity

We examined whether myosin II ATPase is involved in the glutamate-induced DA-actin exodus. In the presence of aBL, drebrin localization at dendritic spines was not affected by glutamate stimulation (photomicrographs in Fig. 7), and glutamate stimulation did not induce a decrease in drebrin SDR (n = 30 cells; p = 0.06, Student's *t* test; graph in Fig. 7). Interestingly, the actin SDR was slightly, but significantly, decreased upon glutamate stimulation (graph in Fig. 7), although the decrease was not remarkable compared with that in the presence of iBL (Fig. 7). This result indicates that inhibition of myosin II ATPase does not completely block the exodus of F-actin, indicating that a small amount of F-actin other than DA-actin exits dendritic spines in response to glutamate stimulation.

Together, it is indicated that the glutamate-induced as well as the cLTP-induced DA-actin exodus depends on myosin II ATPase, but the glutamate-induced non-DA-actin exodus is at

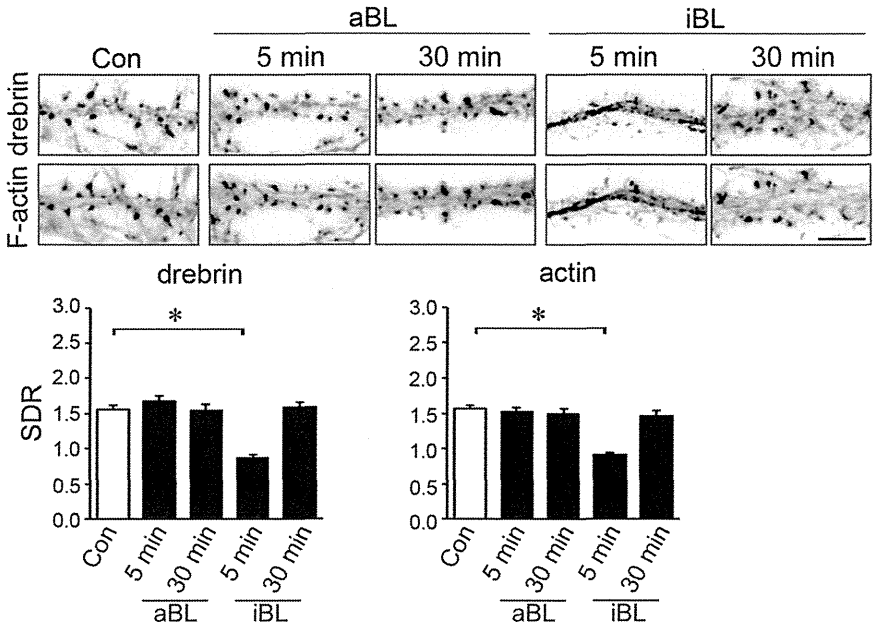

Figure 4. cLTP-induced DA-actin exodus is blocked by an inhibitor of myosin II ATPase. Neurons (21 DIV) were preincubated with 100 μM (S)-(−)-blebbistatin (aBL, the active form of blebbistatin) for 30 min and then stimulated with cLTP solution for 3 min. (R)-(+)-blebbistatin (iBL, the inactive form of blebbistatin) was used as a control. Scale bars, 5 μm. F-actin images indicate that spines kept their structure during the experiment although their shapes were changed. The aBL-treated neurons did not show a decrease in the drebrin and actin SDRs at either 5 min or 30 min after cLTP stimulation (n = 30 cells; Student's test), whereas iBL-treated neurons showed a significant decrease in the drebrin and actin SDRs at 5 min (n = 30 cells; $p<0.01$, Scheffe's test), similar to that observed in control neurons in Fig. 3. Error bars represent s.e.m.
doi:10.1371/journal.pone.0085367.g004

least partly independent of myosin II ATPase. This myosin II-independent loss of non-DA-actin might correspond to the NMDA receptor-independent loss of non-DA-actin shown in Fig. 6A.

The DA-actin exodus is not dependent on phosphorylation of myosin light chain

To examine whether the phosphorylation of myosin light chain (MLC) is involved in the DA-actin exodus, we inhibited myosin

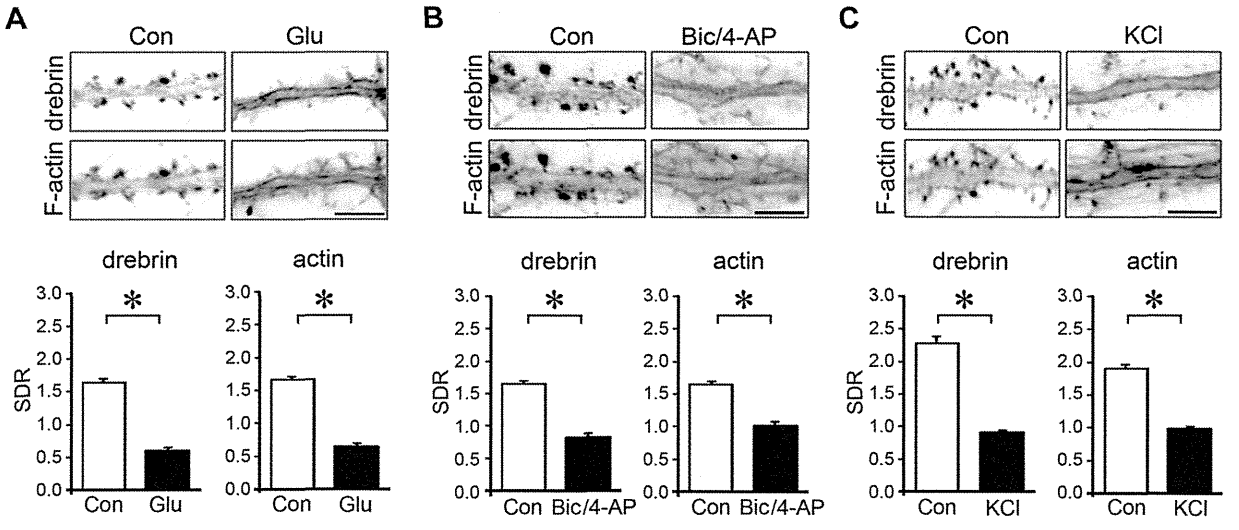

Figure 5. Effects of various excitatory stimulations on DA-actin distribution. Images were obtained from neurons (21 DIV) double-labeled for drebrin and F-actin. Bar graphs represent the spine-dendrite ratios (SDRs) for drebrin and actin. (**A–C**) Neurons were stimulated with 100 μM glutamate for 10 min (A), 50 μM bicuculline and 500 μM 4-aminopyridine (Bic/4-AP) for 10 min (B), or 90 mM KCl in Tyrode's solution for 5 min (C). F-actin images indicate that spines kept their structure during the experiment although their shapes were changed. After stimulation, the drebrin and F-actin clusters in the spines disappeared, and a linear staining pattern appeared along the dendrite. Both the drebrin and actin SDRs were significantly decreased (glutamate, n = 170 cells; Bic/4-AP, n = 30 cells; KCl, n = 30 cells; $p<0.01$, Student's *t* test). Note that the control drebrin and actin SDRs in (C) were greater than the other SDRs because Tyrode's solution was used instead of normal medium. Scale bars, 5 μm. Error bars represent s.e.m.
doi:10.1371/journal.pone.0085367.g005